The Astrophysical Journal, 939:101 (16pp), 2022 November 10 https://doi.org/10.3847/1538-4357/ac9673

Ultra-diffuse Galaxies as Extreme Star-forming Environments. II. Star Formation and Pressure Balance in H I-rich UDGs

Erin Kado-Fong, Chang-Goo Kim, Jenny E. Greene, and Lachlan Lancaster
Department of Astrophysical Sciences, Princeton University, Princeton, NJ 08544, USA; kadofong@princeton.edu
Received 2022 July 6; revised 2022 September 23; accepted 2022 September 27; published 2022 November 10

Abstract

In addition to occupying the extreme, diffuse tail of the dwarf galaxy population, ultra-diffuse galaxies (UDGs) are themselves a key laboratory in which to study star formation in extreme low-density environments. In the second paper of this series, we compare the spatially resolved star formation activity of 22 H I-selected UDGs and 21 "normal" dwarf galaxies within 120 Mpc to predictions within the pressure-regulated, feedback-modulated (PRFM) theory of star formation. To do so, we employ a joint spectral energy distribution fitting method that allows us to estimate star formation rate and stellar mass surface density from UV-optical imaging. We find that the PRFM framework extends successfully to the UDG regime—although the UDGs in our sample show unusually low star formation rate surface densities given their H I content, this low star formation efficiency can be naturally explained by the diffuse structure of the UDGs. In fact, when cast in the PRFM framework, the relationship between midplane pressure and star formation in the UDG sample is in good agreement not only with the "normal" dwarf reference sample, but also with measurements from more massive galaxies. Our results suggest that despite their low star formation efficiencies, the H I-rich UDGs need not be forming stars in an exotic manner. We also find that the UDGs are likely H_2 poor compared even to the overall dwarf population.

Unified Astronomy Thesaurus concepts: Low surface brightness galaxies (940); Dwarf galaxies (416); Star formation (1569)

1. Introduction

Star formation and galaxy evolution are intrinsically linked processes; a full understanding of one is not possible in the absence of a theory of the other. In addition to the most definitional link—that star formation grows stellar mass while consuming gas—the resulting feedback from star formation also has a direct impact on the structure of the galaxy's interstellar medium (ISM) via processes including supernovae, UV radiation, and stellar winds (see, e.g., Kim et al. 2013, 2017; Girichidis et al. 2018; Kannan et al. 2019; Kim et al. 2021; Lancaster et al. 2021). In order to understand how and why galaxies evolve the way that they do—especially at the low-mass end, where star formation feedback is expected to play an outsized role (see, e.g., Dekel & Silk 1986; Silk 1997; El-Badry et al. 2016; Behroozi et al. 2019; Hu 2019; Dashyan & Dubois 2020; Smith et al. 2021), we must understand the self-regulatory process of star formation. Likewise, to understand the environments in which star formation proceeds, we must understand the arc of galaxy evolution through cosmic time.

In both the fields of star formation and galaxy evolution, we seek out "extreme" cases in order to best test and stretch our understanding of the underlying physical processes at work. Ultra-diffuse galaxies (UDGs) are dwarf galaxies characterized by large stellar sizes and low surface brightnesses. Though exact definitions vary, UDGs are typically required to have effective radii greater than 1.5 kpc and central surface brightnesses fainter than 24 mag arcsec^{-2} (see Van Nest et al. 2022 for an overview of UDG definitions). These diffuse galaxies are extreme as both a product of galaxy evolution and as an environment in which stars form. Indeed, the study of UDGs as an extreme sector of the dwarf galaxy population has enjoyed both extensive observational (see, e.g., Sandage & Binggeli 1984; McGaugh et al. 1995; Dalcanton et al. 1997; van Dokkum et al. 2015; Beasley & Trujillo 2016, 2016; Peng & Lim 2016; Yagi et al. 2016; Leisman et al. 2017; Greco et al. 2018a, 2018b; van Dokkum et al. 2018; Danieli et al. 2019; Janowiecki et al. 2019; van Dokkum et al. 2019; Gault et al. 2021; Danieli et al. 2022; Greene et al. 2022) and theoretical (e.g., Amorisco & Loeb 2016; Di Cintio et al. 2017; Chan et al. 2018; Jiang et al. 2019; Liao et al. 2019; Wright et al. 2021; Van Nest et al. 2022) study. However, less work has been devoted to their star formation properties.

UDGs are extreme environments for star formation due to their presumably low stellar mass surface densities and likely shallow potential wells; see, for example, Leisman et al. (2017) and Kong et al. (2022) for studies of UDGs in the field. Typical halo masses for UDGs in clusters are a topic of significant debate: see, e.g., van Dokkum et al. (2015), Beasley & Trujillo (2016), van Dokkum et al. (2019), Sales et al. (2020), and Saifollahi et al. (2021). These conditions are a marked departure from those of the solar neighborhood or even the outer (Milky Way) disk that serve as the fiducial environment for many models of star formation (Krumholz et al. 2009; Ostriker et al. 2010). Mapping out the star formation activity in UDGs thus serves as a test of the extensibility of these star formation models to new and extreme diffuse conditions.

In the first paper of this series (Kado-Fong et al. 2022; hereafter referred to as Paper I) we demonstrated that UDGs form stars inefficiently relative to their H I surface densities (where SFE(H I) $\equiv \Sigma_{\rm SFR}/\Sigma_{\rm HI}$) on scales down to 500 pc. However, a study of the atomic gas alone is insufficient to understand whether this low SFE(H I) is unexpected given the diffuse structure of the

UDGs. In Paper I we demonstrated that the star formation in UDGs is different from that of normal dwarfs, but in this paper we will consider whether that difference in star formation can be explained by our understanding of the physical processes that drive and modulate star formation.

To this end, we turn to the pressure-regulated, feedback-modulated model of star formation that has been developed over a series of works (Ostriker et al. 2010; Kim et al. 2011; Ostriker & Shetty 2011; Kim et al. 2013; Kim & Ostriker 2015) and most recently condensed into Ostriker & Kim (2022). This theory establishes a link between star formation rate surface density and weight ($\mathcal{W}$) by considering the role of star formation feedback in maintaining the structure and energy density (pressure) of the ISM. This physical relationship provides us with a method that links the two notable features of the UDGs in this work—their unusual structure and their low star formation rate surface density. With this framework in hand, we will endeavor to explain the surprising—or perhaps expected—nature of the star formation in H I-rich UDGs.

We will structure the paper as follows, and note that readers familiar with either Paper I or PRFM star formation may feel free to skip certain sections. In Section 2 we will summarize the data and methods that we utilized in Paper I to produce the initial data products used in this analysis. We will then give an abbreviated overview of PRFM star formation theory in Section 3, before moving onto a discussion of its application to the dwarfs at hand in Section 4. Finally, we will discuss the implications of the analysis on our understanding of the structure and star formation of UDGs in Section 5.

2. Data Sets

Readers familiar with Paper I of this series will find that this content has been covered in greater detail in Paper I and may skip to Section 3. We provide the most salient points of our sample here for those readers not familiar with the first paper of this series, but encourage those readers with an interest in the methods to refer to Paper I for a more in-depth discussion of the analysis therein.

Our dwarf sample consists of two main branches: a high surface brightness, "normal" dwarf sample drawn from the H I catalog of Bradford et al. (2015), hereafter the NSA sample, and a UDG sample with known distances from the H I catalog of Janowiecki et al. (2019). The NSA sample is drawn from the NASA Sloan Atlas, a catalog of nearby galaxies reanalyzed from the Sloan Digital Sky Survey (SDSS) DR8 (Aihara et al. 2011; Blanton et al. 2011). The UDG sample was selected to have a maximum distance of $d = 120$ Mpc; we enforce the same limit on the NSA sample. We note that in this work we will refer to the "normal" galaxy sample as the NSA sample, as these galaxies were not specifically chosen to exclude low surface brightness galaxies. Rather, their relatively high surface brightnesses are a result of the observational selection that led to their inclusion in the NSA.

2.1. Sample Overview

Let us first define the UDG sample. We draw our galaxies from the H I-selected catalog of Janowiecki et al. (2019), selecting those which have five-band imaging from the Hyper Suprime-Cam Subaru Strategic Program (HSC-SSP; Aihara et al. 2019, 2022). Drawing from an H I-selected sample, at least in the regime of the low surface brightness UDGs, comes with two key advantages for the study of star formation in low-density conditions. First, the galaxies selected via H I observations tend to be relatively isolated, which is quite key given the large influence that environment—and particularly the presence of massive galaxies—plays on star formation in low-mass galaxies (see, e.g., Geha et al. 2012; Carlsten et al. 2022). We find that one UDG in our sample, AGC227965, is quenched (star formation rate, SFR $< 10^{-3}$ $M_\odot$ yr^{-1}) presumably due to being a close satellite of MRK1324. We leave this galaxy in our analysis as it still yields a significant H I detection, but note that our discussion of the star formation models does not apply to this system due to the ongoing interaction. Second, and perhaps most importantly for the low surface brightness regime, an H I-selected sample has redshift measurements from the 21 cm line, which allows us to determine distances to relatively isolated UDGs. This selection results in a total sample of 21 H I-selected UDGs.

In order to make a fair assessment of the star formation activity of the UDGs, we also draw a reference sample of 32 NASA Sloan Atlas (NSA) dwarfs at $d < 120$ Mpc with H I measurements from Bradford et al. (2015) to act as a "normal" dwarf reference sample. For this work, we consider the 21 NSA dwarfs with stellar masses of no greater than $M_\star = 3 \times 10^8\, M_\odot$ (the maximum stellar mass covered by the UDG sample). This results in a median stellar mass of $\langle \log_{10}(M_\star/M_\odot)\rangle_{50} = 8.0$ for the NSA sample and $\langle \log_{10}(M_\star/M_\odot)\rangle_{50} = 7.9$ for the UDG sample.

In Figure 1 we show the galaxies in our sample in stellar mass versus H I mass (left), SFR versus H I mass (center), and the star-forming main sequence (SFMS, right). These results are obtained via the spectral energy distribution (SED) fitting method presented in Paper I that we will summarize in Section 2.2. In this figure and all subsequent figures, we show the NSA sample in purple and the UDG sample in red. The results of the Leroy et al. (2008) sample of nearby galaxies and SDSS spectroscopic value-added catalog (Kauffmann et al. 2003; Brinchmann et al. 2004; Salim et al. 2007) are shown in beige and gray, respectively. We find that the UDGs have high H I masses for their stellar masses, and that they have low SFRs for their H I masses.

2.2. SED Fitting

In order to understand the star formation of UDGs down to 500 pc scales, we must devise a method in which to measure their star formation on the relevant physical scales. In the absence of spectroscopic or narrowband measurements—both of which are hindered, but not rendered impossible, by the low surface brightness of the UDGs—we turn instead toward a joint UV-optical SED fitting method that combines the star formation information from Galaxy Evolution Explorer (GALEX) far-ultraviolet (FUV) and near-ultraviolet (NUV) with the spatial resolution of the Hyper Suprime-Cam Subaru Strategic Program (HSC-SSP) optical imaging, which attains a median seeing of $0\farcs77$ in the g band (Aihara et al. 2019). The GALEX imaging is over a factor of 6 lower in spatial resolution, with an FUV and NUV point-spread function (PSF) FWHM of $4\farcs2$ and $4\farcs9$, respectively. Convolving the HSC optical imaging to GALEX seeing would clearly constitute an unreasonable degradation of the optical imaging. We have thus developed an SED fitting process that jointly models global UV and spatially resolved optical photometry.

A full description of the SED fitting process and validation can be found in Paper I and we direct the interested reader to this work. We also present a schematic layout of the procedure in Figure 2.

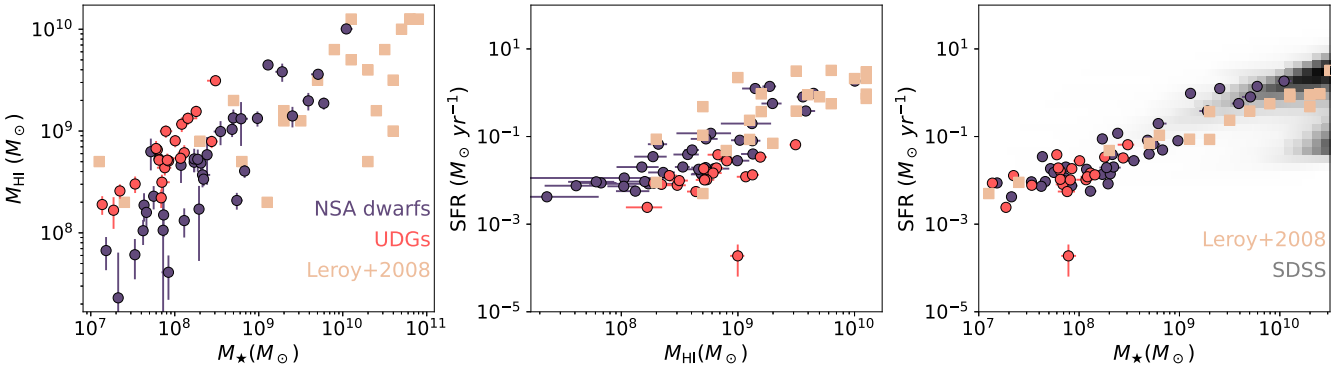

Figure 1. A comparison of the integrated properties of the samples derived in this work against the directly measured result of Leroy et al. (2008; beige points). In all panels, the red points show UDGs and the purple points show NASA Sloan Atlas (NSA, our "normal" dwarf comparison sample—see text) dwarfs. From left, we show the relationship between stellar mass and H I mass, the relationship between H I mass and SFR, and the star-forming main sequence (SFMS). In the SFMS panel, we also show the results of the SDSS DR7 MPA-JHU added-value catalogs in grayscale (Kauffmann et al. 2003; Brinchmann et al. 2004; Salim et al. 2007). We find a good agreement between our results and those from the literature. Although the UDGs have high H I masses for their stellar mass (left panel), they have relatively little SFR for their H I mass (middle panel).

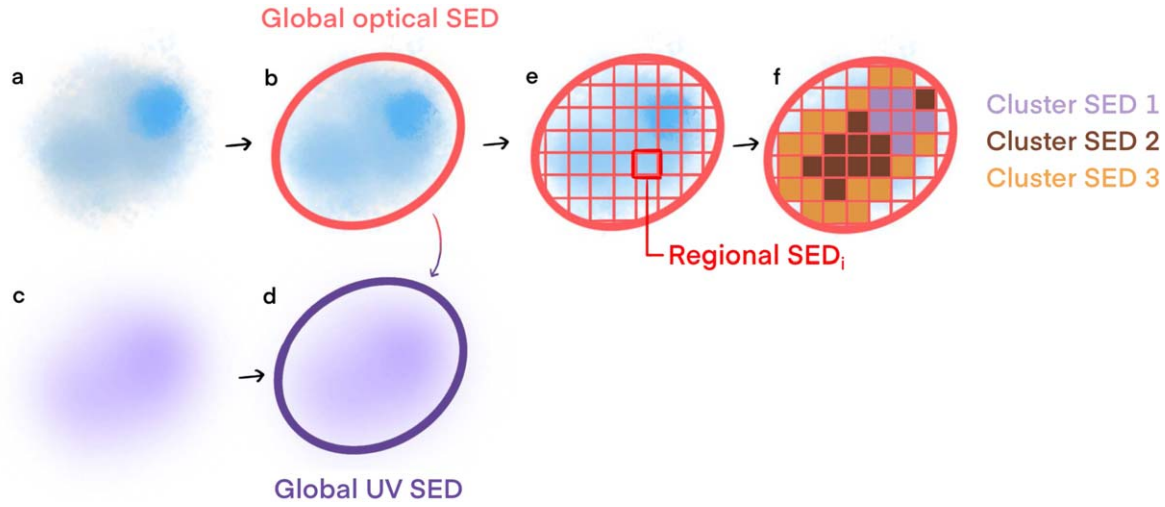

Figure 2. A schematic layout of the fitting technique used in this work, as introduced in Paper I. At left, we show a schematic representation of the optical data and UV data in panels (a) and (c), respectively. In this analysis, the UV data are at much lower spatial resolution than the optical data. We then illustrate the global SED fit of the optical and UV data in (b) and (d); the apertures here are held fixed over the UV and optical data. We then divide the optical data into regions in which regional SEDs are measured (panel (e)). Panel (f) shows the clustering of these spatial regions into three representative "clusters"; these cluster SEDs will be fit jointly with the global UV photometry of panel (d).

First, let us review the typical assumptions and parameters one must choose when approaching an SED fitting problem. We use a Kroupa initial mass function (IMF) throughout (Kroupa 2001) with the Flexible Stellar Population Synthesis (FSPS) library (Conroy et al. 2009; Conroy & Gunn 2010). For this work, we hold stellar and gas-phase metallicity fixed at $Z = 0.004$ (approximately one-third solar). This choice is motivated by both technical and scientific concerns: first, due to the joint nature of the SED fitting, we would like to minimize the number of parameters fit for each cluster SED (panel f, Figure 2). Second, the mass–metallicity relation is not well understood for these dwarf samples. Direct (T_e) measurements are limited to nearby ($d \lesssim 20$ Mpc) samples of typically "normal" dwarfs (Lee et al. 2006; Berg et al. 2012; Jimmy et al. 2015); these direct measurements can show significant offsets relative to each other and to SED fitting methods used for more distant samples (Bellstedt et al. 2021). We thus choose to adopt a typical value following the literature compilation of Bellstedt et al. (2021) for a galaxy of $M_\star \sim 10^8 M_\odot$. We find in Paper I that our results are not significantly impacted by our assumption of a fixed metallicity; assuming solar metallicity shifts the estimated stellar mass and SFR of our dwarf samples by ∼0.08 dex on average. The star formation rate surface densities and stellar mass surface densities estimated using solar metallicity models are shifted by less than 0.01 dex on average compared to their fiducial values.

We also adopt an exponentially declining star formation history

$$\mathrm{SFR}(t) \propto e^{-(t-t_0)/\tau} \quad (1)$$

for all of the models in this work.

Our SED fitting method uses the emcee implementation of the Markov Chain Monte Carlo method for parameter estimation (Foreman-Mackey et al. 2013). We begin with a joint fit to the UV and optical global photometry; this allows us to estimate the reddening in the galaxy and provides a reasonable point at which to instantiate walkers in the joint fitting step. We then subdivide the galaxy into regions no smaller than twice the FWHM of the PSF in our PSF-matched optical images. These regions are required to have a median signal-to-noise ratio of 3 across the five optical bands. Then, we use K-means clustering in the space of

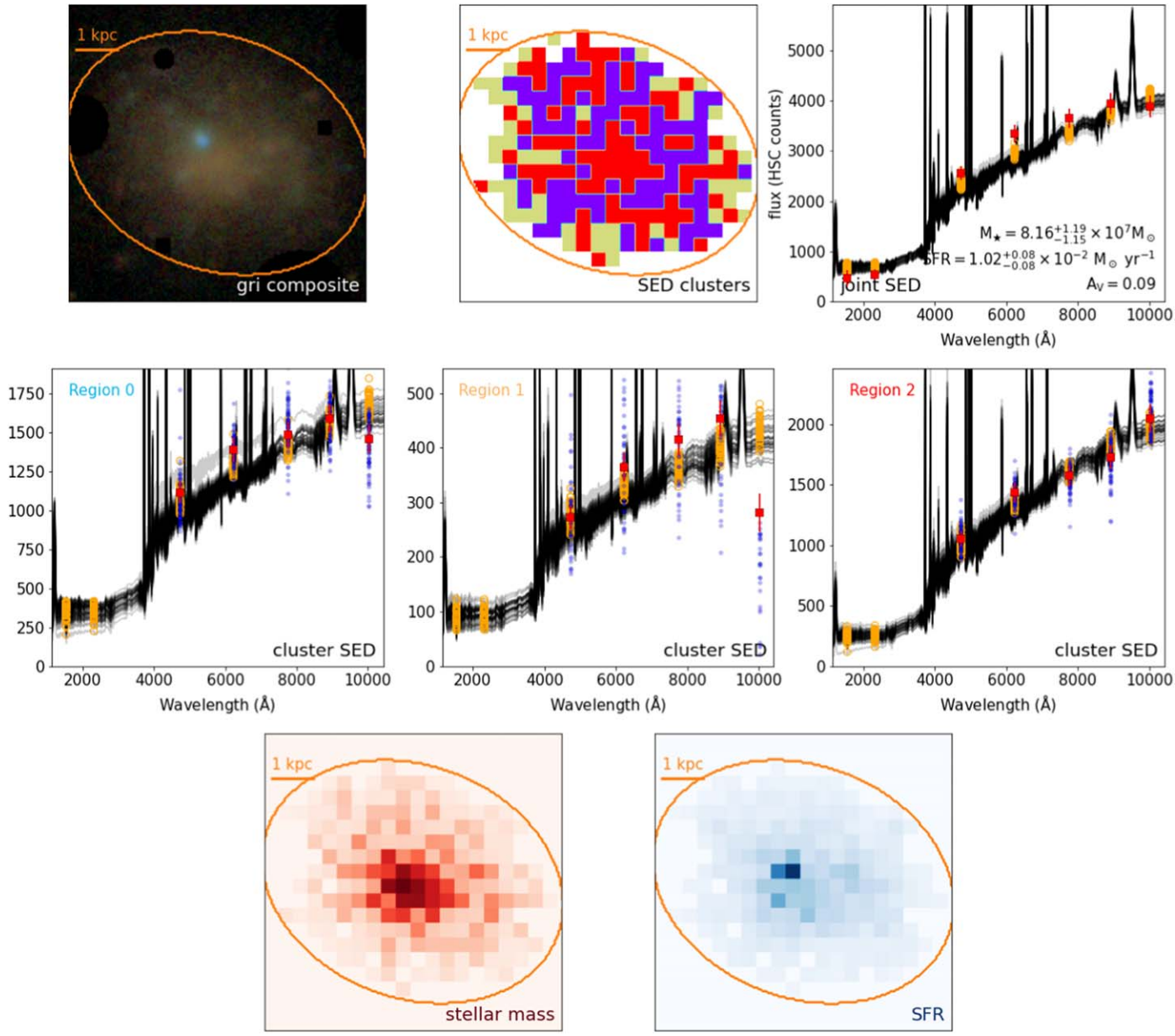

Figure 3. An example of the fitting process for one of the UDGs (AGC 334349). Top row: from left, the HSC *gri*-composite image, the SED cluster map, and the joint UV-optical SED fit. The joint model SED is the result of fitting the spatially resolved (cluster) optical photometry and global UV photometry. The black curves show the model spectra, while the orange points show the model photometry for each filter. The red points show the global UV-optical photometry. The model fitting and figure fluxes are computed as HSC counts. Middle row: optical-only results for the individual cluster SEDs. The color of the title text corresponds to the color of the region in the top middle panel; the format is equivalent to the joint SED fit (top right), with the addition of the SEDs measured in individual spatial regions as blue points. Bottom row: the resultant stellar mass (left) and SFR (right) maps.

optical photometry to assign these regions to clusters that have similar SEDs (Figure 3, top middle panel)—this reduces the number of individual SEDs that we must fit in the joint modeling step. Finally, we fit the global UV data jointly with the cluster optical SEDs (Figure 3, middle row): that is, we adopt the likelihood

$$\log \mathcal{L} \propto -\frac{1}{2}\sum_{i\in UV} \frac{\left(\sum_j^N f_{i,j} - \sum_j^N \hat{f}_{i,j}\right)^2}{\sum_j^N \sigma^2_{f_{i,j}}} + \log\left(\sum_j^N \sigma^2_{f_{i,j}}\right) + -\frac{1}{2}\sum_j^N \sum_{i\in \mathrm{Opt}} \left[\frac{(f_{i,j} - \hat{f}_{i,j})^2}{\sigma^2_{f_{i,j}}} + \log(\sigma^2_{f_{i,j}})\right], \quad (2)$$

where i refers to the bandpass index and j refers to the cluster index. This allows us to jointly fit the spatially resolved optical photometry and the global, unresolved UV photometry. From this inference, we can then immediately extricate the stellar mass surface density, given the amplitude of the cluster SEDs, as well as the star formation rate surface density, which we estimate by integrating the inferred star formation history over the past 100 Myr (Figure 3, bottom row). We choose 100 Myr given that due to our UV coverage, we should be most sensitive to star formation averaged over this time scale.

We finally compute the average stellar mass density and star formation rate surface density over 500 pc, 1 kpc, and global scales. In this step, we require that the averaging scale is larger

than the scale of the regions in which we measure the region SEDs (panel e of Figure 2). In practice, this affects only five galaxies: four are UDGs (AGC 227965, AGC 322019, AGC 198543, and AGC 238961), and one is an NSA dwarf (NSA ID 17750). The results of these galaxies are thus shown on 1 kpc and global scales, but not on 500 pc scales—their exclusion at 500 pc does not constitute a statistically significant impact on our analysis.

3. Background on PRFM Theory

We will summarize the basic points of pressure-regulated, feedback-modulated (PRFM) star formation, but direct the reader to Ostriker & Kim (2022) for an in-depth discussion of the theory.

For a galaxy disk in a quasi-steady state or in vertical dynamical equilibrium, the weight (per unit area) of the ISM should be balanced by the pressure difference between the midplane and the top of the gas layer. Since the pressure is generally decreasing rapidly along the z-axis (perpendicular to the disk plane), the midplane pressure must match the overlying weight. The weight of the ISM, $\mathcal{W}$, is a sum of the contribution by the gas and by the external components (stars and dark matter),

$$\begin{aligned}\mathcal{W} &= \int_0^{z_{\max}} dz\ \rho(g_{\rm gas} + g_{\rm ext}) \\ &= \mathcal{W}_{\rm gas} + \mathcal{W}_{\rm ext},\end{aligned} \tag{3}$$

where $z_{\max}$ refers to the vertical confine of the gas disk, $g_{\rm gas}$ and $g_{\rm ext}$ are the vertical components of the gravitational field due to the gas and the external gravitational potential, and $\mathcal{W}_{\rm gas}$ and $\mathcal{W}_{\rm ext}$ are the corresponding weight components.

Assuming slab geometry, it can be shown that the weight from the gas gravity is $\mathcal{W}_{\rm gas} = (\pi G \Sigma_{\rm gas}^2)/2$, where $\Sigma_{\rm gas}$ is the total gas surface density. If the external gravity dominates, we can approximate the weight as $\mathcal{W}_{\rm ext} = \Sigma_{\rm gas}\sqrt{2G\rho_{\rm sd}}\,\sigma_{\rm eff}$, where $\rho_{\rm sd}$ is the combined density of stars and dark matter, and $\sigma_{\rm eff}$ is the effective vertical velocity dispersion of the gas. This effective velocity dispersion includes the turbulent, thermal, and magnetic contributions. To estimate the weight from observables, we take a simplified form called the dynamical equilibrium pressure $P_{\rm DE}$ that is obtained by combining the two weight contributions as introduced in Ostriker & Kim (2022):

$$\mathcal{W} \approx P_{\rm DE} = \frac{\pi G \Sigma_{\rm HI}^2}{2} + \Sigma_{\rm HI}\sqrt{2G\rho_{\rm sd}}\,\sigma_{\rm eff}. \tag{4}$$

This approximation is good to within ≈20% (see Ostriker & Kim 2022 for a more complete derivation of the full weight expression), and has been adopted in the literature to estimate the total weight from observable quantities (see, e.g., Sun et al. 2020). The reader will note that we have made a notable change to the construction of $\mathcal{W}$. We do not have molecular gas estimates for our samples, and thus take the base assumption that these galaxies are H I-dominated and that the molecular gas is a minor contributor to the total gas mass of the ISM. That is, we assume $\Sigma_{\rm gas} \approx \Sigma_{\rm HI}$. We assume a $\sigma_{\rm eff} = 10\,{\rm km\,s^{-1}}$, as in previous works (see, e.g., Sun et al. 2020). This assumption is reasonable for the dwarf samples at hand as $\sigma_{\rm eff}$ is likely dominated by the warm gas sound speed.

Having laid out an observational estimate of the weight (that is, the dynamical equilibrium pressure), which is an estimate of the total midplane pressure, we now want to make a connection between the total pressure and star formation activity. Total pressure here is defined as the sum of contributions from thermal pressure, turbulent pressure (vertical Reynolds stress), and vertical Maxwell stress as $P_{\rm tot} = P_{\rm th} + P_{\rm turb} + \Pi_{\rm mag}$. Each of these pressure terms is expected to be linked to star formation activity: thermal pressure scales largely with the mean FUV field intensity, turbulent pressure is sourced by momentum injection from supernovae, and magnetic pressure —though relatively less well understood—is thought to scale to some degree with turbulent kinetic pressure via galactic dynamo.

A great deal of work has been devoted to quantifying the relationship between these pressure terms and star formation activity. The key parameter quantifying this relation is the "feedback yield," defined as

$$\Upsilon_{\rm X} \equiv \frac{P_{\rm X}}{\Sigma_{\rm SFR}} \tag{5}$$

where X refers to a given pressure component. In particular, Ostriker & Shetty (2011) showed that the turbulent pressure is related to SFR surface density as $P_{\rm turb} = p_\star/(4m_\star)\Sigma_{\rm SFR}$, where $p_\star$ is the spherical momentum injection per supernova and $m_\star$ is the total mass of stars formed per star that will become a supernova. For a typical IMF (e.g., Kroupa 2001), $m_\star \approx 100 M_\odot$. Recently, 3D supernova-driven bubble expansion simulations have converged to a characteristic value of $p_\star/m_\star \sim 1000$–$3000\,{\rm km\,s^{-1}}$, giving rise to $\Upsilon_{\rm turb} \sim 250$–$750\,{\rm km\,s^{-1}}$. This value is insensitive to the background density and metallicity (e.g., Iffrig & Hennebelle 2015; Kim & Ostriker 2015; Martizzi et al. 2015; Kim et al. 2017; Fielding et al. 2018; Oku et al. 2022).

Turning our attention to the thermal pressure, it is established that $P_{\rm th}$ should scale with the FUV field intensity as the photoelectric heating (e.g., Bakes & Tielens 1994; Weingartner & Draine 2001) is the dominant heating source, which is dependent on both $\Sigma_{\rm SFR}$ and attenuation from the ISM. In particular, a scaling relation can be written for $\Upsilon_{\rm th}$ with respect to solar neighborhood conditions as:

$$\begin{aligned}\Upsilon_{\rm th}(f_\tau, \Sigma_{\rm HI}, Z_d') &= 240\ {\rm km\ s^{-1}} \\ &\times \frac{4.1 f_\tau / f_{\tau,\odot}}{1 + 3.1\left(\frac{\Sigma_{\rm HI} Z_d' f_\tau / f_{\tau,\odot}}{10\ M_\odot\ {\rm pc^{-2}}}\right)^{0.4}},\end{aligned} \tag{6}$$

where we assume a dust metallicity of $Z_d' = Z/Z_\odot = 1/3$, in line with our SED fitting assumptions. We also introduce f_τ, which is the mean attenuation factor of the UV radiation field. Under the assumption of slab geometry and uniform gas and source distribution, the radiation transfer solution is

$$f_\tau \equiv \frac{1 - E_2(\tau_{\rm FUV}/2)}{\tau_{\rm FUV}}, \tag{7}$$

where $E_2(n)$ is the second exponential integral and $\tau_{\rm FUV}$ is the mean FUV optical depth in the direction perpendicular to the disk. We estimate $\tau_{\rm FUV}$ for our galaxies by computing $A_{\rm FUV}$ assuming a Calzetti (2013) extinction curve and the A_V inferred from our global SED fits. Ostriker et al. (2010) showed that for solar neighborhood–like conditions one arrives at $\Upsilon_{\rm th} \approx 240\,{\rm km\,s^{-1}}$ (see Equation (15) of Ostriker et al. 2010, or,

equivalently, Equation (12) of Ostriker & Kim 2022). We compute somewhat higher values of $\Upsilon_{\rm th}$ for the present samples due to lower Σ and lower Z' than those of solar neighborhood, with a median value of $\Upsilon_{\rm th} \sim 660\,{\rm km\,s^{-1}}$ at 1 kpc scales.

It is generally expected that the saturation level of the magnetic stress is set by a fraction of the turbulent stress (e.g., $\Upsilon_{\rm mag} \sim 0.5 - 1.0\Upsilon_{\rm turb}$; Kim & Ostriker 2015). However, the quantitative prediction may still depend on the details of galactic dynamo. In this work, we adopt a fiducial $\Upsilon_{\rm turb} = 500\,{\rm km\,s^{-1}}$ and a scaling of $\Upsilon_{\rm mag} = 0.75\Upsilon_{\rm turb}$.

We thus arrive at a theoretical PRFM prediction of

$$\Upsilon_{\rm tot} = \frac{P_{\rm tot}}{\Sigma_{\rm SFR}} \sim 875\ {\rm km\ s^{-1}} + \Upsilon_{\rm th}(f_\tau, \Sigma_{\rm HI}). \quad (8)$$

Numerical results from the TIGRESS[1] framework (Kim & Ostriker 2017) validate the theoretical assumptions of the PRFM theory and calibrate $\Upsilon_{\rm tot}$ as a function of $P_{\rm DE}$ as (Ostriker & Kim 2022, Equation (25c)):

$$\log_{10}\left(\frac{\Upsilon_{\rm tot}}{\rm km\ s^{-1}}\right) = -0.212\log_{10}\left(\frac{P_{\rm DE}}{k_B\ {\rm cm^{-3}\ K}}\right) + 3.86. \quad (9)$$

Given a method to compute $\Upsilon_{\rm tot}$ (we will use the numerical prescription of Equation (9), but will include a comparison to Equation (8) in Section 4.5), the PRFM prediction for SFR surface density is

$$\Sigma_{\rm SFR} = \frac{P_{\rm DE}}{\Upsilon_{\rm tot}}, \quad (10)$$

where the right-hand side is composed of our observable quantity ($P_{\rm DE}$) and the theoretical/numerical prediction ($\Upsilon_{\rm tot}$).

From here, we will consider whether the markedly low SFE (H I) of our observed UDG sample can be explained within the framework of PRFM star formation.

4. Results

Having provided the reader with a brief introduction to PRFM theory, we may now proceed to the application of this framework to the present sample. Before we jump headlong into the computation, however, it is of substantial importance to first justify that the PRFM theory of star formation is applicable to our dwarf samples, and how we will go about estimating the parameters necessary to predict star formation within the model framework.

4.1. The Validity of PRFM Assumptions for the Present Sample

A preliminary question that we must first address before applying the PRFM model to the sample at hand is whether the equilibrium disk assumptions that lie at the heart of the theory are satisfied in our low-mass systems. In this work, we are averaging both spatially (over at least 500 pc) and temporally (over approximately 100 Myr, given that GALEX FUV is included in the SED fitting). The equilibrium assumption is valid if either the averaging time scale or length scale is large enough to average over deviations from equilibrium. In this section, we will provide an argument that our averaging time scale is long enough to justify the equilibrium assumption, but we note that the spatial averaging is also likely sufficient to validate the equilibrium assumption. Indeed, it should be noted that spatial averaging allows PRFM theory to be used for star formation tracers that track SFR on shorter timescales than our time-averaging arguments may otherwise imply (e.g., Hα, which traces star formation activity on $\sim$10 Myr timescales).

Before moving onto these time-scale arguments, however, it is worth considering whether these dwarfs are well described by gaseous disks. There is substantial evidence from H I rotation curves that dwarfs (including UDGs) in this mass range do host H I disks (Hunter et al. 2012; Greco et al. 2018a; Mancera Piña et al. 2019, 2020; Gault et al. 2021; Mancera Piña et al. 2022). There are, to the authors' knowledge, no published analyses of the stellar kinematics of field UDGs, but there is evidence that UDGs in the field are "puffy" but largely axisymmetric systems characterized by a mean disk thickness of $\sim 0.5R_{\rm d}$, where $R_{\rm d}$ is the disk length (Kado-Fong et al. 2021). We thus generally find long-lived disks for the galaxies in our sample, so the slab geometry assumption of PRFM is reasonable for the present work. We then must carefully consider the assumptions of thermal and dynamical equilibrium due to proposals that dwarfs have generally bursty star formation histories, and that UDGs in particular may be formed via particularly bursty histories (Di Cintio et al. 2017; Chan et al. 2018).

The thermal equilibrium assumption of the PRFM model may be disrupted if the cooling and heating timescales are so long that the majority of the gas is out of equilibrium. In this case, the gas would not promptly respond to the change in the heating rate and hence the star formation rate. We can estimate the validity of this assumption by comparing the time scale over which we measure the star formation rate to the cooling and heating time for these dwarfs, which quantifies the time it takes to re-establish a thermal equilibrium. In particular, let us write the cooling and heating time of warm gas as:

$$t_{\rm cool} = \frac{k_B T_w}{n\Lambda} = \frac{k_B T_w}{\Gamma}, \quad (11)$$

where k_B is Boltzmann's constant, $T_w \sim 5000$–8000 K is the temperature of the warm gas, and $n\Lambda$ and Γ are the cooling and heating rate per particle, respectively. With $\Gamma \sim 5 \times 10^{-27}$–$10^{-26}\,{\rm erg\,s^{-1}}$, appropriate for low-metallicity gas (Wolfire et al. 2003), we have a cooling time of $t_{\rm cool} \sim 2$–6 Myr. This cooling time is significantly shorter than the time scale over which we measure our star formation rates (100 Myr)—thus, the time scale over which our measurement is averaging is larger than the cooling time by roughly an order of magnitude. This indicates that even the smallest regions over which we are averaging (500 pc) should follow the equilibrium expectation.

Variations in star formation can also drive large-scale changes in the dynamical equilibrium structure of the galaxy (El-Badry et al. 2016; Orr et al. 2019). We can quantify the degree to which dynamical equilibrium is a valid assumption for the system under consideration here by comparing the time scale over which we measure the SFR to the vertical crossing time of the disks, which generally quantifies the time over which excess kinetic energy is dissipated in the galaxy (Ostriker et al. 2001). Generally, we can write $t_{\rm cross} \approx H_{\rm gas}/\sigma_{\rm eff}$, where $H_{\rm gas}$ is the gas scale height. We estimate the

[1] Three-phase Interstellar medium in Galaxies Resolving Evolution with Star formation and Supernova feedback.

gas scale height as

$$H_{\rm gas} = \frac{2\sigma_{\rm eff}^2}{\pi G \Sigma_{\rm HI} + 2\sigma_{\rm eff}\sqrt{2G\rho_{\rm sd}}}, \quad (12)$$

which is equivalent to Equation (5) of Ostriker & Kim (2022) except that we assume $\Sigma_{\rm gas} \approx \Sigma_{\rm HI}$ and take $W \approx P_{\rm DE}$. This estimate results in $t_{\rm cross} \approx 30$ Myr for the samples at hand—again, significantly smaller than the time scale over which we are measuring star formation activity.

4.2. Estimating ρ_{sd}

Having addressed these assumptions, we now proceed to the sample at hand. In order to estimate $P_{\rm DE}$ (Equation (4)), we will need an estimate for the midplane density of stars ($\rho_\star$) and dark matter ($\rho_{\rm dm}$), $\rho_{\rm sd} = \rho_\star + \rho_{\rm dm}$. We estimate the stellar mass density at the midplane as $\rho_\star = \Sigma_\star/(2H_\star)$, where $H_\star$ is the disk scale height and $\Sigma_\star$ is the stellar mass under the assumption of an exponential density profile.

We obtain this estimate statistically by using the measured scale lengths of our galaxies in conjunction with the three-dimensional shape distributions inferred by Carlsten et al. (2021) for the NSA dwarf sample and by Kado-Fong et al. (2021) for the UDG sample. We assume in both cases that the three-dimensional shape distribution of the galaxy sample measured at one effective radius is the same as the distribution measured at the scale length $l_\star$. That is to say that we assume $C/A \approx H_\star/l_\star$, where C/A indicates the ratio between the smallest and largest principle axes of the ellipsoid that describes the galaxy shape distribution at one effective radius, and $H_\star$ and $l_\star$ are the stellar scale height and length, respectively. Both the UDGs (Kado-Fong et al. 2021) and the "normal" dwarfs (Kado-Fong et al. 2020) are well characterized by exponential surface brightness profiles, meaning that $R_{\rm eff} \approx 0.6 l_\star$ assuming a constant stellar mass-to-light ratio. We can then estimate the probability distribution function of $H_\star$ as:

$$\Pr[H_\star] = (2\pi\sigma_{C/A}^2)^{-1/2} \times \exp\left[\frac{-(H_\star/l_\star - \mu_{C/A})^2}{(2\sigma_{C/A}^2)}\right] \quad (13)$$

where $\mu_{C/A}$ and $\sigma_{C/A}$ are the inferred mean and standard deviation of the bivariate Gaussian used to describe that intrinsic shape distribution in Carlsten et al. (2021) and Kado-Fong et al. (2021).

We use the Carlsten et al. (2021) 3D shapes because of the overlap in stellar mass between the two samples, but we note that their sample is composed only of satellite galaxies. We therefore also compute $\Sigma_{\rm SFR}$ predictions using the 3D intrinsic shape distribution of Kado-Fong et al. (2020), which is incomplete at the relevant stellar masses but includes field galaxies, and find no significant difference in the SFR predictions between the assumptions of intrinsic shape distribution.

We opt to not implement inclination corrections for our sample because the stellar disks are not thin and because empirical results suggest that there is significant variation in the three-dimensional shapes and thicknesses of the dwarf stellar disks (Kado-Fong et al. 2020; Carlsten et al. 2021); however, we compute inclination estimates using the mean disk height-to-length ratio following Holmberg (1958) and find that our results would not qualitatively change if we did implement such an inclination correction. We note that adopting an inclination correction would systematically lower the stellar mass surface density and star formation rate surface density estimates in this work by an average of ∼34% below fiducial values, though we stress that this value is highly uncertain due to the assumptions made in the application of the Holmberg (1958) correction. Furthermore, because the feedback yield $\Upsilon_{\rm tot}$ is the ratio between the midplane pressure and the star formation rate surface density, the effect of an inclination correction applied to both the stellar mass and star formation rate surface density estimates should be lessened.

We now move on to the estimation of the dark matter density, $\rho_{\rm dm}$. Here, we must adopt a dark matter halo profile for each galaxy. This component is by far the most uncertain ingredient in the star formation prescription—not only do we not have any constraint on the individual dark matter halos in which these galaxies live, the overall stellar-to-halo mass relation is highly uncertain for low-mass galaxies. In order to take into account the scatter and uncertainty in the stellar-to-halo mass relation at these masses, we compute the predicted star formation rate using three different dark matter halos: a fiducial best-guess halo mass using the stellar-to-halo mass relation of the FIRE-2 simulations (which predicts halo masses of between 1.6×10^{10} and 6×10^{10} $M_\odot$ for the sample at hand; Hopkins et al. 2018), a halo with $M_h = 10^{12}$ $M_\odot$, and a halo with $M_h = 10^9$ $M_\odot$. We assume a Navarro–Frenk–White (NFW) profile for all dark matter halos in this work (Navarro et al. 1997). We assign a concentration based on the concentration–mass relation of Child et al. (2018). We assign the uncertainty due to the dark matter density to be the difference between $\rho_{\rm dm}$ estimated for a very massive ($M_h = 10^{12}$ $M_\odot$) and very low-mass ($M_h = 10^9$ $M_\odot$) halo, as it is unlikely that any of our galaxies are living in halos with a stellar-to-halo mass ratio more extreme than 0.1 (in the case of the extreme low-mass halo) or 0.0001 (in the case of the extreme high-mass halo). For our fiducial halo assumptions, the combined stellar and dark matter density tends to be dominated by dark matter, as is expected for these low-mass galaxies (see, e.g., Oh et al. 2011). The UDGs tend to be more dark matter dominated, with a median $\rho_\star/\rho_{\rm sd} = 0.14$ compared to the mildly dark matter dominated NSA dwarfs (median $\rho_\star/\rho_{\rm sd} = 0.46$).

We show the distribution over $\rho_{\rm sd}$ for our fiducial dark matter halo assumption in Figure 4. We find that the NSA dwarfs are characterized by systematically higher values of $\rho_{\rm sd}$, which is unsurprising given that the UDGs are characterized by relatively low stellar surface densities.

4.3. P_{DE} Estimates

Having estimated both $\Sigma_{\rm HI}$ and $\rho_{\rm sd}$, we may now arrive at an estimate of the dynamical equilibrium pressure ($P_{\rm DE}$). We compute this quantity following Equation (4).

Before considering the full PRFM prediction, it is of interest to first consider how $P_{\rm DE}$ varies between the NSA and UDG samples. We show the overall distribution of $P_{\rm DE}$ at each spatial scale used in this work (500 pc, 1 kpc, and global) for each sample in Figure 5. We find that there is no significant variation in $P_{\rm DE}$ distribution as a function of spatial scale, but that the UDGs tend to have lower dynamical equilibrium pressures than do the NSA dwarfs. This result is as expected due to the low $\rho_{\rm sd}$ values of the UDGs (see Figure 4). The

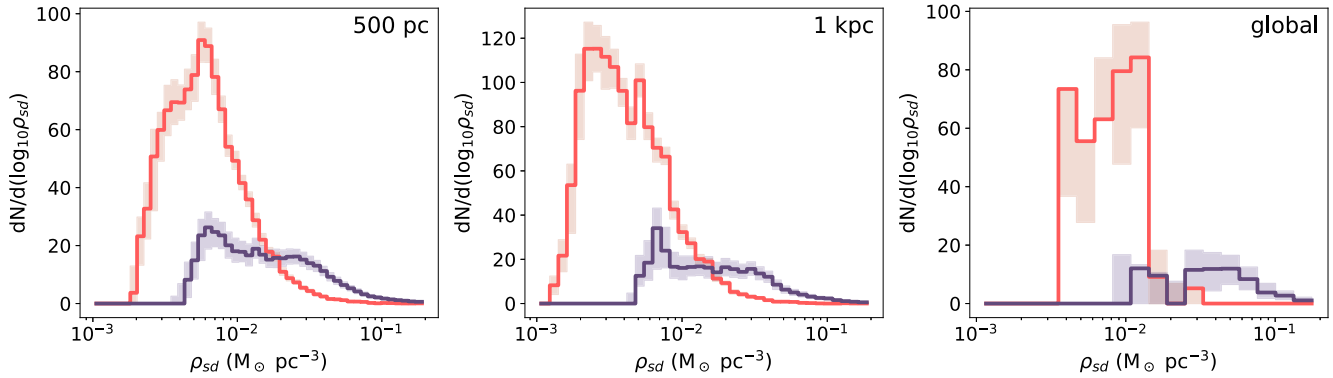

Figure 4. The distribution over ρ_{sd} for our fiducial dark matter halo assumptions (see text) for the NSA dwarfs (purple) and UDGs (red) at 500 pc, 1 kpc, and global scales from left to right. The shaded regions are bounded by the 16th to 84th percentiles of the distribution. The NSA dwarfs are characterized by systematically higher stellar+dark matter densities, which is unsurprising given that the UDGs are characterized by low stellar surface densities.

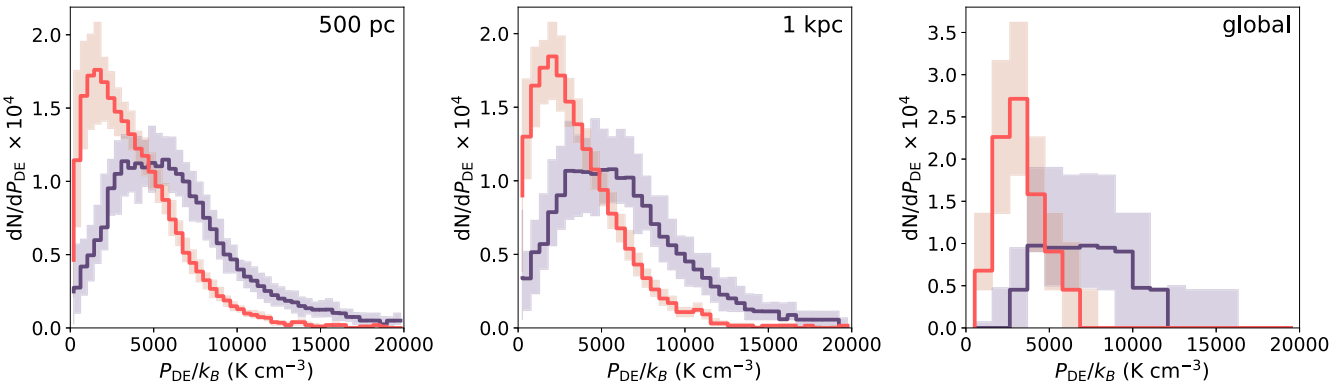

Figure 5. The distribution over P_{DE} for the NSA dwarfs (purple) and UDGs (red) at 500 pc, 1 kpc, and global scales from left to right. The shaded regions at 500 pc and 1 kpc are bounded by the 16th to 84th percentiles of the distribution. We find no significant variation in P_{DE} as a function of spatial scale, but find that the NSA dwarfs have systematically higher dynamical equilibrium pressures than the UDG dwarfs.

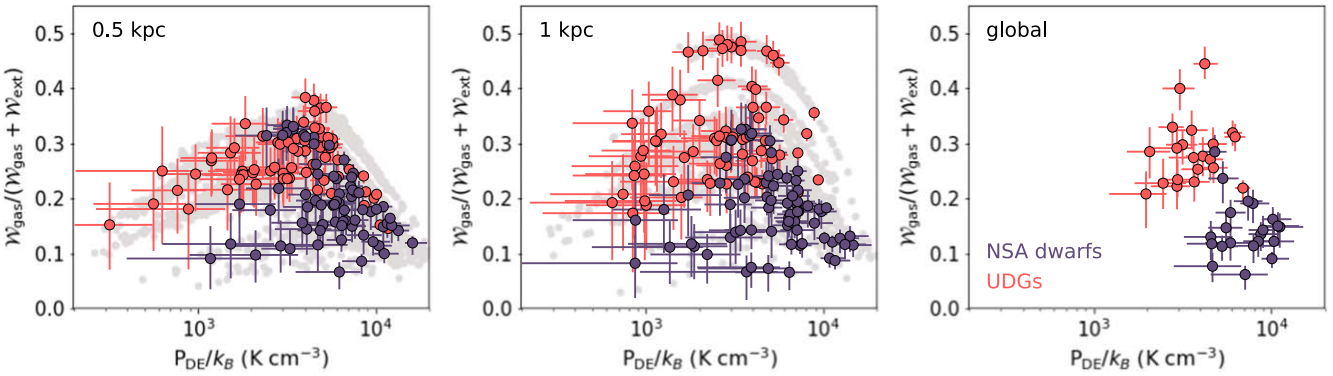

Figure 6. The contribution of self-gravity to the total midplane weight ($\mathcal{W}_{gas}/\mathcal{W}$) as a function of dynamical equilibrium pressure (P_{DE}) as a function of spatial scale (500 pc to global average, from left to right). We show individual error bars for a random sample of regions from the UDG sample (red) and the NSA sample (purple); the full sample is shown in gray. Note that the tracks visible in the left and middle panels are a result of the median assumed H I profiles; the uncertainty in the H I profiles results in a larger dispersion in $\mathcal{W}_{gas}/\mathcal{W}$ than is implied by the tracks alone (as is shown by the error bars of the colored points). We find that the external weight ($\mathcal{W}_{ext}$) is relatively less important in the UDGs as compared to the NSA dwarfs.

relatively low stellar+dark matter densities (and relatively similar H I surface densities) of the UDGs also imply that $\mathcal{W}_{gas}$ is a larger contributor to $\mathcal{W}$ in the UDGs than it is in the NSA dwarfs.

We show $\mathcal{W}_{gas}/\mathcal{W}$ in Figure 6 as computed from Equation (4) where $\mathcal{W} \approx P_{DE}$ and $\mathcal{W}_{gas} = (\pi G \Sigma_{HI}^2)/2$. Each panel shows the dynamical equilibrium pressure versus the fraction of $\mathcal{W}$ contributed by $\mathcal{W}_{gas}$. From left to right, the panels show measurements at 500 pc, 1 kpc, and global scales. For visual clarity, we only show error bars for a random subset of the regions measured in this work. The colored points show a random sample of UDG regions (red) and NSA regions (purple) with their error bars included; the full sample is shown by the gray scatter. The tracks visible in the left and middle panels are a result of the median H I profiles we assume for the galaxies; the uncertainty in these profiles results in a wider dispersion than is implied by the tracks (as shown by the vertical extent of the error bars). Indeed, we find that $\mathcal{W}_{gas}$ accounts for a larger fraction of the total weight in the UDGs than it does in the NSA dwarfs.

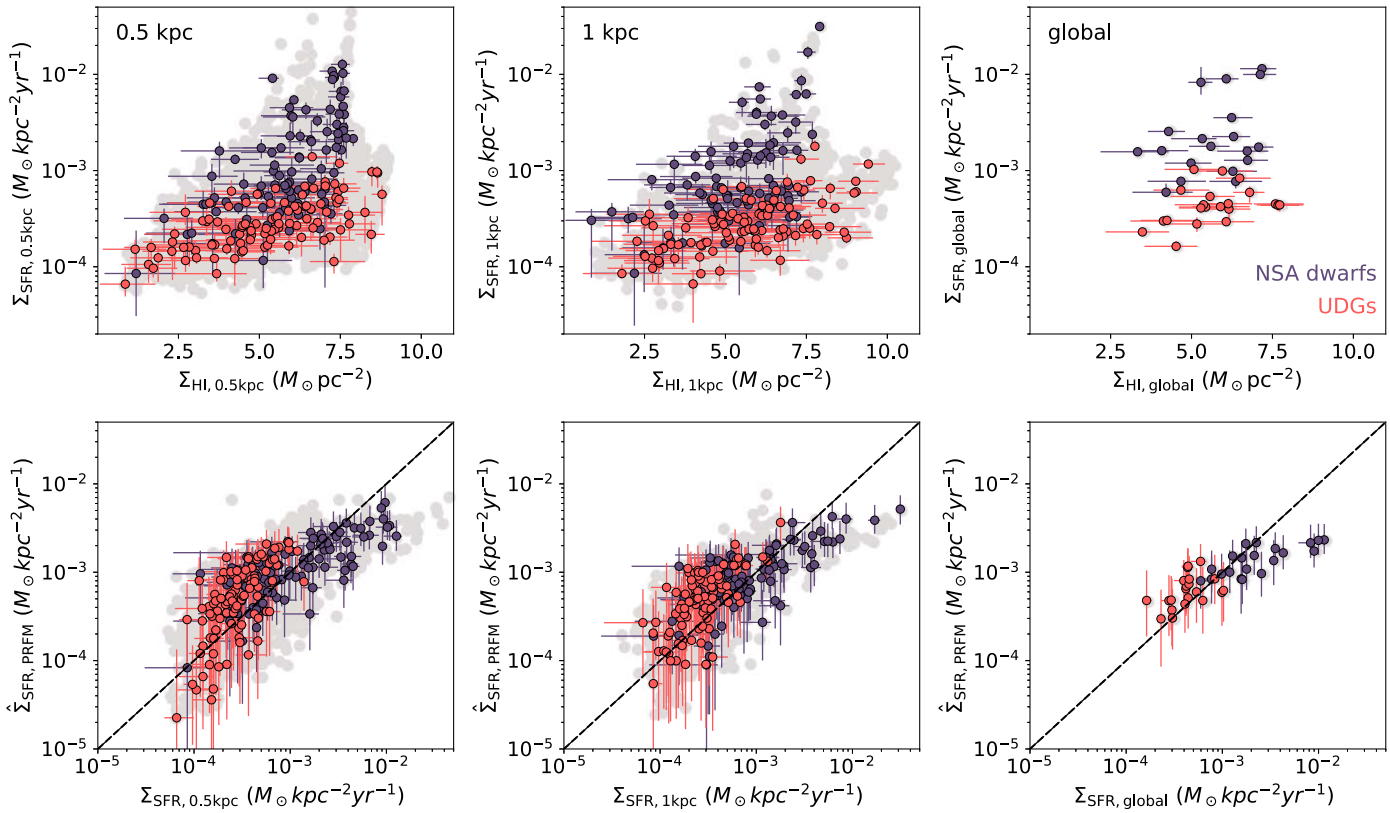

Figure 7. Top row: a comparison between H I surface density estimates and SFR surface density measurements at 500 pc (left column), 1 kpc (middle column), and global scales (right column). In all panels, we only show NSA galaxies that are within the stellar mass range of the UDG sample. For visual clarity, we show a random subset of (at most) 70 points for each sample with individual error bars and colored by sample source; we show the full sample as the underlying gray scatter. Bottom row: a comparison between the observed SFR surface densities and the PRFM predictions. Again, red points show UDGs, while purple points show NSA dwarfs.

4.4. PRFM Predictions

With the assumptions validated and parameters estimated, we may now move on to predicting Σ_{SFR} from the PRFM framework for our observed galaxies. We base our predictions upon the numerically estimated form of Υ_{tot} presented by Ostriker & Kim (2022) using the TIGRESS simulations, as discussed in Equation (9).

In the top row of Figure 7, we show the relationship between Σ_{SFR} and H I surface density for our NSA dwarfs (purple) and UDGs (orange) averaging over 500 pc regions, 1 kpc regions, and the full area of the galaxy. As was shown in more detail in Paper I, the UDGs form stars at consistently lower efficiencies (relative to their H I content) relative to the NSA dwarfs.

We then show the relation between the observed and predicted star formation rate surface densities in the bottom row of Figure 7 for 500 pc, 1 kpc, and global averages. We find that the PRFM prescription succeeds in reproducing the star formation rate surface density measurements of the UDGs at all spatial scales probed, which we will explore quantitatively via a comparison between the predicted and measured values of Υ_{tot} in the following section. The prescription underpredicts Σ_{SFR} for the most vigorously star-forming regions of the NSA sample—this underprediction can be understood if one considers that the NSA dwarfs may have considerable stores of molecular hydrogen (see, e.g., Leroy et al. 2008; de los Reyes & Kennicutt 2019). The discrepancy is most obvious in the globally averaged estimates, which is due to the global averages acting as a Σ_{SFR}-weighted average (where the most vigorously star-forming regions dominate the total mean signal). We also see that the H I-only PRFM predictions perform best for the NSA dwarfs at 500 pc scales, which is consistent with the picture where much of the galaxy is dominated by atomic hydrogen (over molecular hydrogen, as has been suggested previously in, e.g., Leroy et al. 2008). Nonetheless, we find that PRFM theory well describes the majority of the regions within both galaxy samples and thus naturally predicts the low SFE(H I) of the H I-rich UDGs as a consequence of their low ISM weight.

4.5. Empirical Estimates of Υ_{tot}

Finally, though we have adopted Υ_{tot} as a way to predict Σ_{SFR}, it is also informative to reframe the computation as a comparison between the theoretically predicted values for Υ_{tot} (Equations (8) and (9)) and empirically derived Υ_{tot} as the ratio between our observed Σ_{SFR} measurements and P_{DE} estimates. In this way, we can quantitatively compare the relationship between star formation and dynamical equilibrium pressure in our dwarf samples and similar measurements of more massive galaxy samples from the literature within the context of theoretical expectations.

Because the theoretical Υ_{tot} depends explicitly upon τ_{FUV} (Equation (7)), we compute a running median predicted Υ_{tot} for our sample as a function of P_{DE} in bins of width 0.1 dex. The shaded region in each panel spans the 16th to 84th percentiles of the theoretical Υ_{tot} prediction over the same domain.

We show such a comparison in Figure 8. At left, we show Σ_{SFR} versus P_{DE} at 500 pc, 1 kpc, and global scales with the predictions using Υ_{tot} overplotted (Equation (8) solid,

Equation (9) dashed). At right we show the empirical estimate for $\Upsilon_{\rm tot}$ as a function of $P_{\rm DE}$, again with both the theoretical and numerical predictions for $\Upsilon_{\rm tot}$ shown in brown. Here, we show the median value of $\Upsilon_{\rm tot}$ for the UDG and NSA samples as the red and purple points, respectively, and depict the range between the 16th and 84th percentiles in both $P_{\rm DE}$ and $\Upsilon_{\rm tot}$ as solid unfilled rectangles of the same color. For the reader's convenience, we tabulate these values in Table 1. For comparison, we also show empirical $\Upsilon_{\rm tot}$ estimates inferred from the literature results of PHANGS (orange dotted–dashed box; Sun et al. 2020), EDGE-CALIFA (blue dotted–dashed box; Barrera-Ballesteros et al. 2021), and KINGFISH (green dotted–dashed box; Herrera-Camus et al. 2017). We show the same literature results in each panel, but note that these measurements are taken on the scale of $\sim$1 kpc. We also note that the literature measurements take H_2 into account in their computation of $P_{\rm DE}$.

Directing the reader's attention first to the top and middle rows (500 pc scales and kiloparsec scales, respectively), we see that both the empirically derived $\Upsilon_{\rm tot}$ measured from the UDG sample and NSA sample are in good agreement with the predictions of Ostriker & Kim (2022). We moreover see that the empirically derived $\Upsilon_{\rm tot}$ of both dwarf samples at kiloparsec and lower scales are in good agreement with the measured $\Upsilon_{\rm tot}$ values of the literature samples of more massive galaxies (which do have H_2 incorporated in their $P_{\rm DE}$ estimates). This is to say that, as quantitatively measured by $\Upsilon_{\rm tot}$, the relationship between our estimate of ISM weight and star formation appears to be relatively constant between "extreme" (low-density) dwarfs, "normal" dwarfs, and their much more massive counterparts. When we consider globally averaged values, we find that the median empirical $\Upsilon_{\rm tot}$ measured for the NSA dwarfs drops significantly—this may be suggestive of a significant store of H_2 in these NSA dwarfs, which we will discuss further in Section 5.2.

Encouragingly, we find that the empirically measured $\Upsilon_{\rm tot}$ values derived from the dwarf samples on $\leqslant$1 kpc scales are in good agreement with both the theoretical and numerical predictions for $\Upsilon_{\rm tot}$ presented in Ostriker & Kim (2022). However, a unified analysis of a sample that includes high $P_{\rm DE}$ regions ($P_{\rm DE} \sim 10^5 k_B$ K cm^{-3}) would be necessary to expand quantitatively upon the numerical expectation of a $P_{\rm DE}$ dependence beyond the simple literature comparison presented in this work.

5. Discussion

5.1. Star Formation Efficiency in UDGs

In Paper I, we demonstrated that UDGs host relatively low star formation rate surface densities given their apparent H I surface densities. In this work, we have gone on to consider whether this low efficiency star formation is surprising in the context of contemporary theories of galactic star formation. As we have detailed in the preceding section, we find that the pressure-regulated, feedback-modulated (PRFM) theory of star formation is remarkably successful at predicting the low $\Sigma_{\rm SFR}$ and SFE(H I) of the UDGs. The star formation in these "extreme" galaxies, then, can be well described within the same framework of PRFM star formation as can the "normal" (NSA) dwarfs and even more massive galaxies—the difference in their star formation behavior can be quantitatively attributed to the shallower gravitational potential due to the characteristically diffuse stellar structure of the UDGs.

The bottom panels of Figure 7 demonstrate that the PRFM model is highly successful at reproducing the star formation rate surface densities of the UDGs, even without considering the surface density contribution of molecular gas. Furthermore, Figure 8 shows that the NSA dwarfs and UDGs lie on the same relation between $P_{\rm DE}$ (dynamical equilibrium pressure) and $\Sigma_{\rm SFR}$ as do massive galaxies. These successes indicate that H I-rich UDGs, which are largely in the field, need not be forming stars in an exotic manner, as has been suggested for globular cluster rich UDGs in high-density environments (Danieli et al. 2022).

Beyond a direct comparison of observed and predicted star formation rate surface densities, the PRFM framework allows us to quantitatively explore the relationship between star formation and galaxy structure in our samples. We make observational estimates of $\Upsilon_{\rm tot}$ in Section 4.5 to compare our results to both theoretical expectations and observational measurements of higher-$P_{\rm DE}$ systems. We find that the median value of $\Upsilon_{\rm tot}$ is about 1000–2000 km s^{-1} (see Table 1). This is consistent with theoretical expectations and similar to previous literature results (though there is significant variation between literature samples, as shown in Figure 8). Our UDG sample is characterized by somewhat higher values of $\Upsilon_{\rm tot}$ and lower values of $P_{\rm DE}$ compared to the NSA sample, which is also consistent with the expectation that the momentum injection from supernovae and FUV heating are more efficient in low-density environments due to weaker cooling and less shielding. However, as we will discuss further in the next section, the $P_{\rm DE}$ estimates of the NSA sample may be biased low due to the neglected contribution from H_2. Thus, the main takeaway from the empirical $\Upsilon_{\rm tot}$ results should be the agreement between theoretical predictions and the low-SFE (H I) UDG sample, rather than the variation between the NSA and UDG samples. The concordance between midplane pressure and star formation rate surface densities in the UDG sample also implies that in the absence of an event that strongly raises $P_{\rm DE}$ (e.g., the accretion of enough high-density gas to overcome the effect of the low stellar mass density on $P_{\rm DE}$), H I-rich UDGs are unlikely to support the bursty and concentrated star formation at $z = 0$ that has been suggested to form UDGs and/or link them to blue compact dwarfs (Di Cintio et al. 2017; Sánchez Almeida et al. 2018). However, a broader view of the mechanisms that trigger and sustain concentrated bursts of star formation in low-mass galaxies is needed to further explore the link between these populations.

Having established the concordance between the results at hand and both theoretical and observational results from the literature, we can also examine the implication of the composition of $P_{\rm DE}$ on predictions of $\Sigma_{\rm SFR}$. Although $\mathcal{W}_{\rm gas}$ is *relatively* more important for the UDGs (than it is for the NSA dwarfs), we also note that $\mathcal{W}_{\rm ext} \geqslant \mathcal{W}_{\rm gas}$ for all of the galaxies and length scales probed. This indicates that the external gravitational potential (from stars and dark matter) plays a significant role in setting the star formation time scale; that is, gas surface density alone is not sufficient to fully predict $\Sigma_{\rm SFR}$. Indeed, a correlation between dwarf stellar mass surface density and divergence from the Kennicutt–Schmidt relation has been demonstrated in samples of nearby galaxies (de los Reyes & Kennicutt 2019; see also the top row of Figure 7). Altogether, these results paint a picture in which galaxy structure, rather than gas availability alone, plays a key role in regulating star formation in low-mass systems.

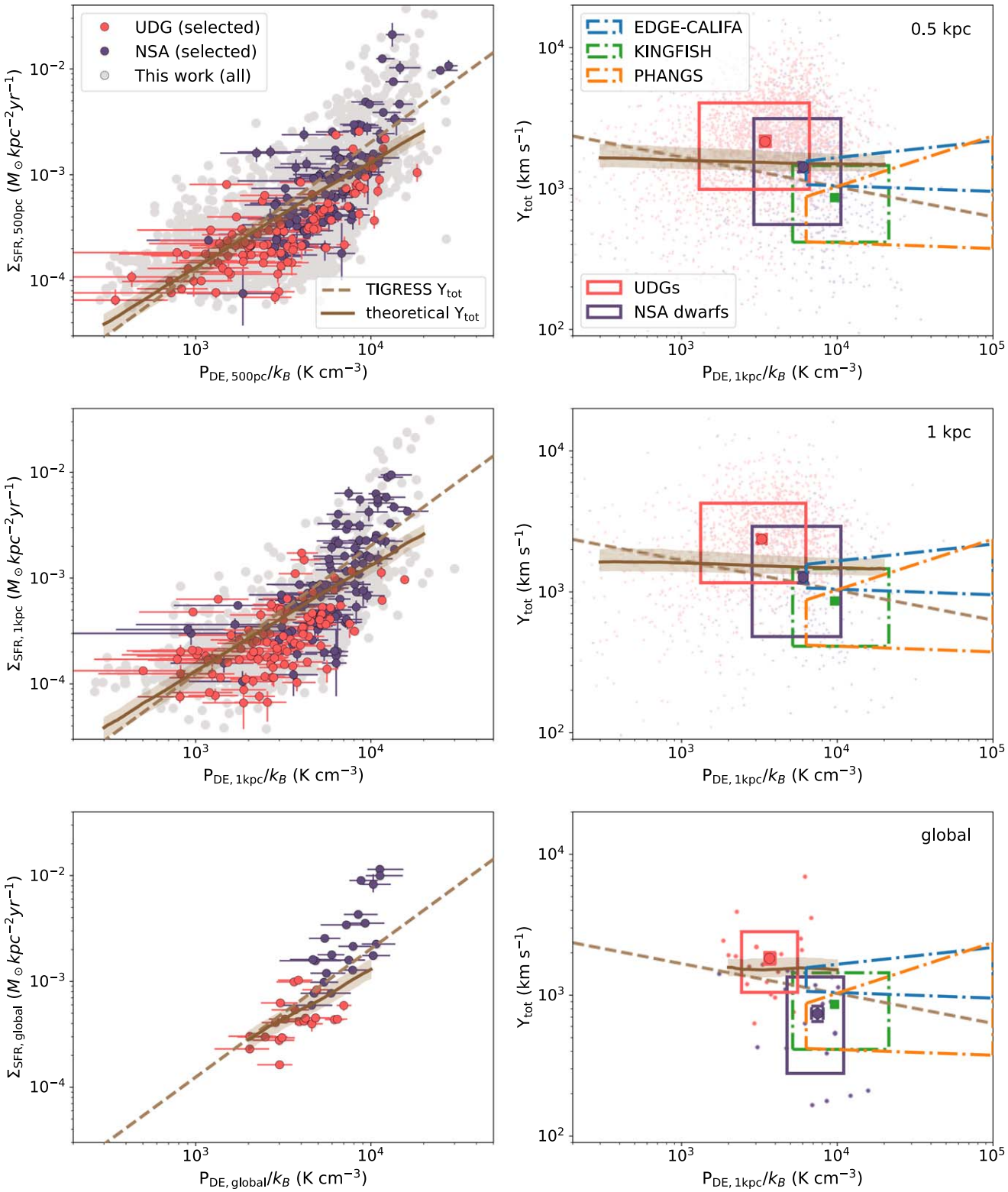

Figure 8. Left: an estimate of the dynamical equilibrium pressure (P_{DE}) for our sample. As in Figure 7, we show a random sample of points with their individual error bars and colors (red for the UDG sample, purple for the NSA sample) and the full sample in gray. We overplot the theoretical (Equation (8)) and numerical (Equation (9)) predictions of Ostriker & Kim (2022) as the dashed and solid lines, respectively. Right: an empirical estimate of Υ_{tot} ($=P_{DE,obs}/\Sigma_{SFR,obs}$) as a function of dynamical equilibrium pressure. We compare to kiloparsec-scale observations from PHANGS (orange dotted–dashed; Sun et al. 2020), EDGE-CALIFA (blue dotted–dashed; Barrera-Ballesteros et al. 2021), and KINGFISH (green dotted–dashed; Herrera-Camus et al. 2017), as well as to the theoretical predictions of Ostriker & Kim (2022).

5.2. Molecular Hydrogen in UDGs

In this work we have shown that the PRFM model of star formation does a remarkably good job of accounting for the star formation rate surface density of the UDGs, despite the fact that we assume that the contribution of molecular hydrogen to the overall weight of the system is negligible. In general and quite separate from the discussion of UDGs, galaxies in this

Table 1
The 16th, 50th, and 84th Percentile Values of $P_{\rm DE}$ and $\Upsilon_{\rm tot}$ for the UDG and NSA Samples

Sample	Scale	$P_{\rm DE}^{16}$ $\left[\frac{10^3 {\rm K}}{k_B\ {\rm cm}^3}\right]$	$P_{\rm DE}^{50}$ $\left[\frac{10^3 {\rm K}}{k_B\ {\rm cm}^3}\right]$	$P_{\rm DE}^{84}$ $\left[\frac{10^3 {\rm K}}{k_B\ {\rm cm}^3}\right]$	$\Upsilon_{\rm tot}^{16}$ $\left[10^3 \frac{\rm km}{\rm s}\right]$	$\Upsilon_{\rm tot}^{50}$ $\left[10^3 \frac{\rm km}{\rm s}\right]$	$\Upsilon_{\rm tot}^{84}$ $\left[10^3 \frac{\rm km}{\rm s}\right]$
UDGs	500 pc	$1.32^{+0.18}_{-0.30}$	$3.42^{+0.28}_{-0.22}$	$6.60^{+0.23}_{-0.22}$	$1.01^{+0.12}_{-0.18}$	$2.13^{+0.17}_{-0.14}$	$4.02^{+0.33}_{-0.26}$
	1 kpc	$1.38^{+0.12}_{-0.26}$	$3.26^{+0.21}_{-0.18}$	$6.29^{+0.20}_{-0.17}$	$1.17^{+0.13}_{-0.20}$	$2.38^{+0.11}_{-0.13}$	$4.27^{+0.28}_{-0.24}$
	global	$2.46^{+0.29}_{-0.33}$	$3.69^{+0.27}_{-0.31}$	$5.36^{+0.39}_{-0.37}$	$1.08^{+0.13}_{-0.15}$	$1.79^{+0.16}_{-0.16}$	$2.75^{+0.26}_{-0.26}$
NSA	500 pc	$3.03^{+0.37}_{-0.43}$	$6.06^{+0.33}_{-0.28}$	$10.55^{+0.86}_{-0.66}$	$0.57^{+0.06}_{-0.07}$	$1.44^{+0.12}_{-0.10}$	$3.16^{+0.35}_{-0.27}$
dwarfs	1 kpc	$2.86^{+0.45}_{-0.53}$	$6.02^{+0.34}_{-0.31}$	$10.42^{+0.76}_{-0.55}$	$0.48^{+0.06}_{-0.07}$	$1.27^{+0.11}_{-0.11}$	$2.86^{+0.30}_{-0.27}$
	global	$4.94^{+0.52}_{-0.54}$	$7.37^{+0.58}_{-0.58}$	$10.65^{+1.26}_{-0.83}$	$0.29^{+0.07}_{-0.06}$	$0.73^{+0.10}_{-0.08}$	$1.33^{+0.18}_{-0.15}$

mass range are thought to be relatively poor in H_2 overall—a recent study suggests that nearby dwarfs with stellar masses of less than $\log_{10}(M_\star/M_\odot) = 8.5$ have a median H_2 fraction of $f_{H_2} \equiv \Sigma_{H_2}/(\Sigma_{H_2} + \Sigma_{HI}) = 0.15$ (de los Reyes & Kennicutt 2019). However, studies have also suggested that dwarfs may be dominated by H_2 in their central regions, despite being H_2 poor in a spatially averaged sense (Leroy et al. 2008). Despite their overall small H_2 content, dwarfs are also thought to preferentially host their molecular gas at small radii, allowing H_2 to contribute significantly to or even dominate the weight of the ISM near the center of the galaxy (Leroy et al. 2008).

In order to understand what we may say about the H_2 content in UDGs, we first consider the impact of our H I-only approach on the NSA sample. In Figure 7, we see that the H I-only PRFM model significantly underpredicts $\Sigma_{\rm SFR}$ for the NSA dwarfs, particularly when we consider the star formation rate surface density averaged over kiloparsec or larger scales. At 500 pc scales, the bulk of the regions are well represented by their PRFM predictions, though a tail toward underpredicted $\Sigma_{\rm SFR}$ at high $P_{\rm DE}$ remains. This can be understood if one considers that the average $\Sigma_{\rm SFR}$ measured within any given region of 500 pc, 1000 pc, or greater size is essentially an SFR-weighted average. At global scales, the most vigorously star-forming regions dominate the average $\Sigma_{\rm SFR}$. At 500 pc, these vigorously star-forming regions are siloed into a relatively small number of points. This transition from a roughly SFR-weighted to a roughly area-weighted scheme can also be seen in the behavior of the median $\Upsilon_{\rm tot}$ estimated for the NSA galaxies as a function of region spatial scale in the right column of Figure 8. At 500 pc, the median empirical $\Upsilon_{\rm tot}$ computed from the NSA dwarfs is in good agreement with the prediction from the TIGRESS simulations of Ostriker & Kim (2022). When we consider the global averages, however, the median empirical $\Upsilon_{\rm tot}$ lies well below the simulation prediction. This behavior is consistent with the picture in which molecular gas makes a significant contribution to the weight in the most vigorously star-forming areas of the NSA dwarfs.

Having established the possible impact of neglecting the H_2 contribution in the NSA dwarfs, we may now consider the UDGs. First, unlike the NSA dwarfs, the PRFM prediction tends to slightly overpredict the star formation rate surface densities of the UDGs as a function of $P_{\rm DE}$. This implies that, holding the dark matter halo properties constant (a point we will return to in the following section), the absence of the weight from the H_2 component does not strongly affect the $\Sigma_{\rm SFR}$ predictions for the UDGs. This is despite the fact that, as shown in Figure 6, the self-gravity of the ISM comprises a larger component of the total midplane weight of the UDGs. The UDGs should thus be relatively more sensitive to the effect of neglecting H_2 gas, as the $\mathcal{W}_{\rm gas}$ scales as the square of the gas surface density (as opposed to $\mathcal{W}_{\rm ext}$, which scales linearly with the gas surface density). Thus, we find that, unlike the NSA dwarfs, the UDGs in our sample are unlikely to host large molecular gas stores.

One simple exercise we can undertake to test the idea that H_2 is a less important contributor to $P_{\rm DE}$ in UDGs than in the NSA galaxies is to make a direct estimate of M_{H_2} from the star formation rate via an assumed depletion time $\tau_{\rm dep}$. Observational support for a constant H_2 depletion time of $\tau_{\rm dep} \sim 1$–3 Gyr has emerged from observational work (see, e.g., Bigiel et al. 2008; Leroy et al. 2008; Bigiel et al. 2011; Schruba et al. 2011, 2012; Leroy et al. 2021), though there is evidence for variation within that range as a function of environment (Utomo et al. 2017). For this test we will assume a constant depletion time of $\tau_{\rm dep} \equiv \Sigma_{H_2}/\Sigma_{\rm SFR} = 1.8$ Gyr following the results of Schruba et al. (2011).

Using this assumed H_2 depletion time, we may directly estimate the expected H_2 surface density from our measured star formation rate surface densities. We can then compute the molecular gas fraction in each region, as shown in Figure 9, where the H_2 fraction is defined as $f_{H_2} = \Sigma_{H_2}/(\Sigma_{H_2} + \Sigma_{HI})$. We indeed find that the UDG expected H_2 fractions are quite low, with a median expected molecular gas fraction of $f_{H_2} = 0.09$ and a 99th percentile expected fraction of $f_{H_2} = 0.31$. Conversely, although the median NSA dwarf region has a relatively low expected H_2 fraction ($f_{H_2} = 0.24$), there is a significant tail to H_2-dominated regions—the 99th percentile expected fraction of the NSA sample is $f_{H_2} = 0.83$.

Using these H_2 surface density estimates within the PRFM prediction framework would clearly be circular, as the quantity of interest ($\Sigma_{\rm SFR}$) is the very quantity that we use to estimate Σ_{H_2}. However, this exercise does provide a separate (though we note not entirely independent) consistency check with our previous claim that the molecular gas stores of the UDGs are a subdominant contributor to the overall gas surface density.

5.2.1. Outlooks on H_2 Detection

Clearly, a direct estimation of the H_2 content of the UDGs in our sample would be immensely powerful in determining whether they are H_2 depleted, and whether their SFE(H_2) is consistent with that of "normal" galaxies. There are two substantial technical hurdles to gaining such an estimation: first, the previously discussed low predicted H_2 masses of the UDGs, and second, the substantial uncertainty in converting between a direct measurement (e.g., of CO(1–0)) and H_2 mass in a UDG-like environment.

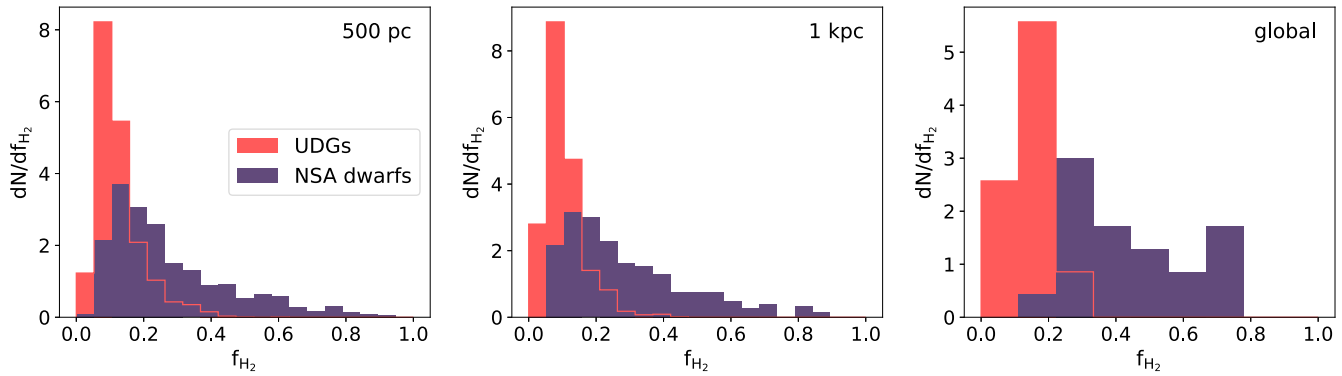

Figure 9. The estimated H_2 fraction (where $f_{H_2} = \Sigma_{H_2}/[\Sigma_{H_2} + \Sigma_{HI}]$) for the regions in our sample at 500 pc (left), 1 kpc (middle), and global scales (right) when we assume a constant H_2 depletion time of $\tau_{dep} = \Sigma_{H_2}/\Sigma_{SFR} = 1.8$ Gyr. The red histograms shows the UDGs, while the purple histograms show the NSA dwarfs. We find that while the distribution in f_{H_2} peaks at $f_{H_2} < 0.2$ for both the UDGs and NSA galaxies, the NSA dwarfs are characterized by a tail to high molecular gas fractions. This finding is consistent with the underprediction of the H I-only PRFM estimate for the highly star-forming regions of the NSA galaxies (as shown in Figure 7).

Given a depletion time τ_{dep}, the relation between the CO (1–0) luminosity and H_2 mass can be written as

$$\alpha_{CO(1-0)} = \frac{M_{H_2}}{L_{CO(1-0)}} = \tau_{dep}\frac{SFR}{L_{CO(1-0)}}. \quad (14)$$

As above, we assume an H_2 depletion time of 1.8 Gyr. It is both observed and theoretically expected that α_{CO} should be sensitive to environmental factors such as (but not necessarily limited to) metallicity, with α_{CO} increasing with decreasing metallicity (e.g., Schruba et al. 2011; Bolatto et al. 2013; Gong et al. 2020). Even if a CO detection can be made, it is therefore also necessary to spectroscopically determine the metallicity in order to obtain an estimate of the H_2 mass, which is in itself observationally difficult given the low surface brightnesses and on-sky sparsity of the UDGs. Previous exercises with similar samples have required moderate (1 hr) integration times with wide (2″) slits on the 8.1 m Gemini South telescope in order to yield gas-phase metallicity measurements (Greco et al. 2018a).

In the absence of a gas-phase metallicity measurement, we can make a simple estimate of the expected CO (1–0) luminosity using existing α_{CO} measurements of our most nearby massive dwarfs, the Large and Small Magellanic Clouds (LMC and SMC, respectively). We adopt the α_{CO} measurements of the LMC and SMC of Schruba et al. (2011)—as the more metal-rich system, adopting the α_{CO} measured for the LMC results in higher CO (1–0) luminosities than does adopting the value measured from the SMC. In Figure 10, we show the expected CO (1–0) luminosities of the galaxies in our sample as a function of luminosity distances given the assumptions detailed above. We additionally show a selection of observed CO (1–0) measurements from the literature for a selection of samples that include low-mass and low-metallicity objects (Schruba et al. 2011; Amorin et al. 2016; Kepley et al. 2016; Gao et al. 2022). We find that although the predicted CO (1–0) luminosities are comparable to L_{CO1-0} measurements of nearby dwarfs, the predicted luminosities are significantly lower than literature measurements made at the distance range of the sample. As a small aside, it may be initially surprising to the reader that the distribution of CO luminosities in the UDG sample is close to that of the NSA dwarfs, given that the H_2 fractions of the UDG sample is much lower. Because we are estimating the mass in molecular hydrogen directly from the integrated star formation rate (see Equation (14)), and because the stellar mass range of the samples are chosen to be the same,

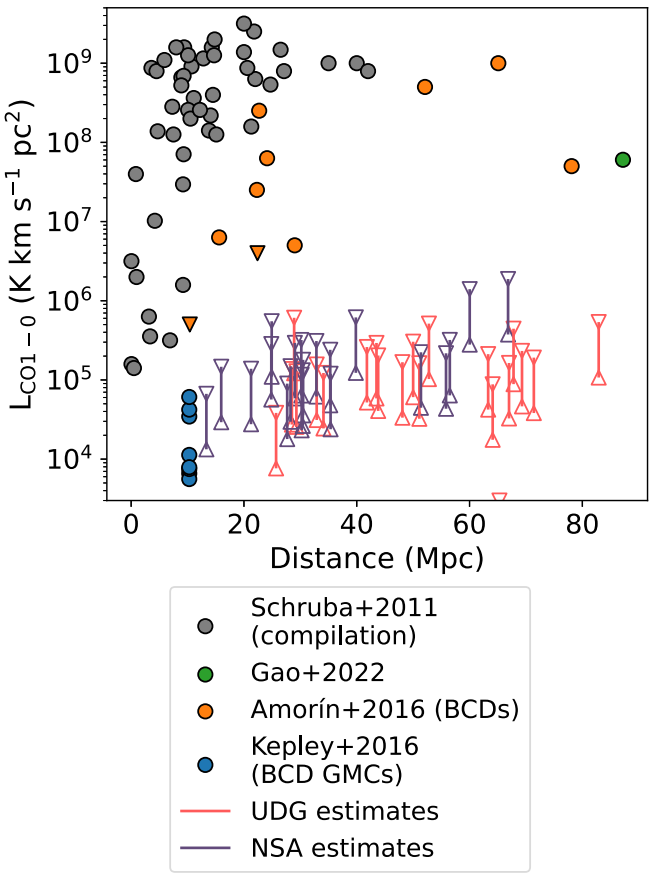

Figure 10. A comparison between the expected CO (1–0) luminosities of our NSA (purple) and UDG (red) dwarf samples and real measurements from the literature. We estimate L_{CO1-0} by assuming a constant H_2 depletion time of $\tau_{dep} = 1.8$ Gyr and bounding our estimates from α_{CO} measurements of the LMC and SMC (Schruba et al. 2011). We find that the expected CO luminosities of the galaxies in the present sample are comparable to measurements made of galaxies at lower distances, but lie well below literature measurements of galaxies at similar distances.

this is essentially a restatement of the result that the UDGs lie on the star-forming main sequence (right panel of Figure 1). The lower H_2 fractions estimated for the UDG sample are then a result of elevated H I masses (at fixed stellar mass) seen in the UDGs versus the NSA dwarfs (left panel of Figure 1).

An alternative approach is to measure the dust mass via SED fitting in the far-infrared, where emission may be modeled as a

modified blackbody with the dust mass, temperature, and emissivity index as free parameters (see, e.g., Kennicutt et al. 2011; Cigan et al. 2021; Shivaei et al. 2022). Due to the distance and mass of the UDGs, it is likely that stacking would be necessary to obtain a robust measurement (Shivaei et al. 2022). The dust mass can then be used to infer to the total gas mass via an assumed dust-to-gas ratio, which can then in turn be used to estimate the H_2 mass given a measured H I mass. However, like α_{CO}, the dust-to-gas ratio is naturally expected to depend on metallicity; measured dust-to-gas ratios at low metallicities also exhibit nonlinearity and substantial scatter (see Figure 11 of Cigan et al. 2021). Thus, deriving a reliable dust-to-gas ratio for these galaxies would be challenging even if metallicity were known.

5.3. If UDGs Live in Special Halos

A rather significant uncertainty in our analysis is the unknown nature of the dark matter halos in which our H I-rich UDGs live. A recent work has shed some light on this topic by estimating halo profile parameters for a sample of H I-rich UDGs (Kong et al. 2022). In this work, the authors suggest that UDGs live in unusually low concentration dark matter halos. Thus, having assumed "normal" dark matter halos for the UDGs—keeping in mind that "normal" is itself an uncertain term for the dwarf population—we may now consider how low concentration halos could impact our results.

There is unfortunately only one galaxy, AGC 242019, that is in both our sample and the sample of Kong et al. (2022). As an exercise, however, we estimate the change in the predicted Σ_{SFR} if we were to adopt the median halo concentration measured by Kong et al. (2022) of $c = 2.62$, which is approximately 30% of the median (16th, 84th percentile) fiducial halo concentration of $c = 9.16$ (8.90, 9.40). We show the impact of this change in the P_{DE}-to-Υ_{tot} plane in the middle panel of Figure 11—assuming the lower concentration halo results in empirical Υ_{tot} values about 25% lower than the fiducial results. We do find that assuming a lower concentration halo nominally brings the UDGs closer in line with theoretical results. However, for the single galaxy that does constitute the overlap between the samples, we find that assuming the halo profile reported by Kong et al. (2022) actually causes a greater difference between our observed and predicted Σ_{SFR}. Indeed, the shift in Σ_{SFR} predictions as a function of halo concentration is more emblematic of the potential effect of unknown systematics in the P_{DE} (and empirical Υ_{tot}) estimates than it is evidence for or against unusual dark matter halo profiles in the UDGs. There thus yet remains significant work to be done in order to reduce the uncertainty of the impact of the UDGs' dark matter halos.

It has also been suggested that some H I-rich UDGs are dark matter deficient based on observations of their neutral gas kinematics (Mancera Piña et al. 2022). It is therefore also useful to understand how the predictions of PRFM theory would change if we were to assume a dark matter density of $\rho_{DM} = 0$. For this exercise, we hold all other estimates fixed to their fiducial values.

We find that the midplane pressure estimates of the UDGs are reduced on average to 59% that of their fiducial values. The midplane pressure estimates of the NSA galaxies, which we compute for completeness, are reduced on average to 73% that of their fiducial values. These reduced values of P_{DE}, and the empirical feedback yields that they imply, remain consistent with PRFM predictions at the precision of our estimates, as shown in Figure 11. We thus do not make a statement about whether $\rho_{DM} = 0$ is a better descriptor of UDG star formation, but rather note that this exercise also indicates that the results presented in this work are not strongly affected by our fiducial choice of halo parameters. This finding is not unexpected given that our estimate of the dynamical equilibrium pressure goes as the square root of the sum of the stellar and dark matter densities, and that the self-gravity term is relatively more important for UDGs (see Figure 6).

6. Conclusions

In this series, we have used spatially resolved SED fitting to explore the star formation activity in a sample of nearby ($d < 120$ Mpc) H I-detected ultra-diffuse dwarf galaxies from Janowiecki et al. (2019), along with a NASA Sloan Atlas (NSA) reference sample of "normal" dwarfs with H I measurements from Bradford et al. (2015). The samples in this work allow us to compare and contrast the star formation behavior of the UDGs with that of the NSA dwarfs, providing new tests for star formation theory in extreme (low-density) environments, as well as new clues to the evolutionary pathway of these H I-rich UDGs (see Paper I).

As established in the first paper of this series, the UDGs are characterized by low star formation rate surface densities and star formation efficiencies (as a function of their atomic gas surface densities) down to 500 pc scales. In this work, we ask whether the UDGs' lower SFE(H I) is expected in the context of contemporary models of star formation.

We consider the framework of pressure-regulated, feedback-modulated star formation (PRFM), which directly connects star formation and galaxy structure for disks in equilibrium, in Section 4. This necessitates an exploration of the dynamical equilibrium pressure in the UDG and NSA dwarf systems. The UDGs are characterized by lower stellar+dark matter densities (Figure 4), lower dynamical equilibrium pressures (Figure 5), and a relatively larger contribution to the overall weight by self-gravity (Figure 6). We indeed find that the lower SFR surface densities and lower SFE(H I) seen in the UDGs are well predicted by the PRFM model; that is, the relationship between midplane pressure and star formation rate surface density (Υ_{tot}) is the same for the UDGs in our sample as it is for the NSA dwarfs, or indeed for even much more massive galaxies.

This holds true for the UDGs despite the fact that we neglect any weight contributions from H_2 in this analysis. We find that at globally averaged scales (which one can think of as the SFR-weighted limit), H I-only predictions underestimate star formation in the NSA dwarfs, but that the same H I-only predictions are in good agreement with the NSA dwarfs at 500 pc scales (which one may roughly think of as approaching an area-weighted average). This implies that H_2 is an important contributor to the weight in the regions of the most vigorous star formation, but is a minority component at large—a suggestion that is in agreement with previous results (see, e.g., Leroy et al. 2008; de los Reyes & Kennicutt 2019). Star formation in the UDGs, however, is well described or even somewhat overestimated by the H I-only PRFM predictions at all spatial scales, suggesting that the UDGs may be H_2 poor even compared to similarly (stellar) massive "normal" dwarfs.

As referenced in Paper I, a clear extension of this work will be to measure spatially resolved H I in a larger sample of field UDGs. In this work, we have also considered routes to estimate H_2 mass

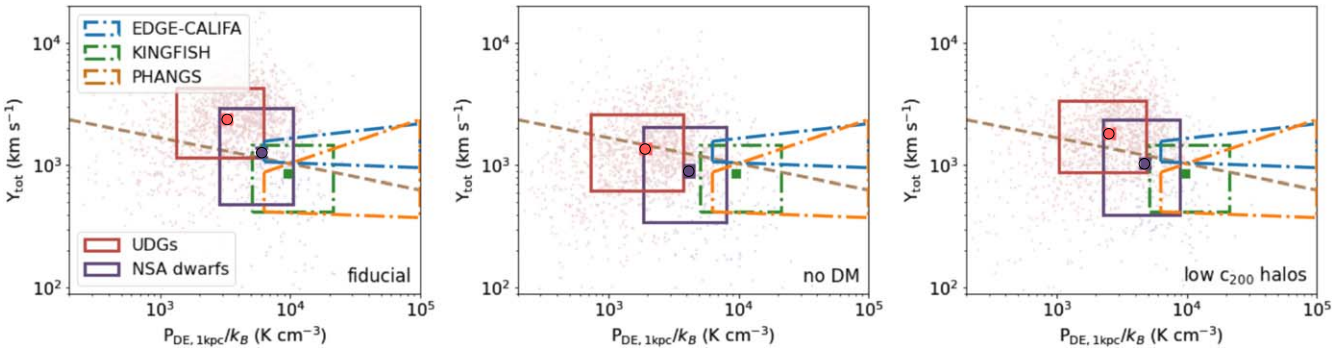

Figure 11. Similar to the right panel of the middle row of Figure 8 but with different assumptions about the halo properties of our sample. We show our fiducial results at left, the empirical feedback yields under the assumption of low concentration halos at middle, and the empirical feedback yields with the assumption that $\rho_{DM} = 0$ at right. We find that our 1 kpc empirical estimates of the feedback yields under the low concentration halo and no-dark-matter assumptions are still consistent with the numerical predictions from TIGRESS. Our results are therefore not inconsistent with low dark matter fractions or low concentration halos in H I-rich UDGs, though we stress that the precision of our estimates precludes us from distinguishing between "normal halo" and "no dark matter" modes of H I-rich UDG structure. This exercise also shows that our results are not strongly dependent on our fiducial choice of a stellar-to-halo mass relation.

in the UDGs, but note that obtaining a detection via either CO or far-infrared dust emission will likely be resource intensive due to the low predicted H_2 fractions and likely low metallicities of the UDGs. The uncertainty in the X_{CO} factor and/or gas-to-dust ratio in these galaxies further increases the uncertainty in obtaining an H_2 mass from such a detection. Nevertheless, a greater understanding of the ISM in UDGs is a key path toward understanding the landscape of star formation in these unusual objects, as well as toward understanding their utility as laboratories in which to study extreme low-density star formation.

The authors thank the anonymous referee for their thoughtful, helpful, and thorough review of this work. The authors thank Eve Ostriker, Song Huang, and Andy Goulding for insightful comments and discussion that have greatly improved this manuscript. The research of E.K.F. was supported by the Porter Ogden Jacobus Fellowship. J.E.G. gratefully acknowledges support from NSF grant AST-2106730. The work of C. G.K. was supported by NASA ATP grant 80NSSC22K0717.

Based in part on data collected at the Subaru Telescope and retrieved from the HSC data archive system, which is operated by Subaru Telescope and Astronomy Data Center at National Astronomical Observatory of Japan.

The Hyper Suprime-Cam (HSC) collaboration includes the astronomical communities of Japan and Taiwan, and Princeton University. The HSC instrumentation and software were developed by the National Astronomical Observatory of Japan (NAOJ), the Kavli Institute for the Physics and Mathematics of the Universe (Kavli IPMU), the University of Tokyo, the High Energy Accelerator Research Organization (KEK), the Academia Sinica Institute for Astronomy and Astrophysics in Taiwan (ASIAA), and Princeton University. Funding was contributed by the FIRST program from Japanese Cabinet Office, the Ministry of Education, Culture, Sports, Science and Technology (MEXT), the Japan Society for the Promotion of Science (JSPS), Japan Science and Technology Agency (JST), the Toray Science Foundation, NAOJ, Kavli IPMU, KEK, ASIAA, and Princeton University.

This paper makes use of software developed for the Large Synoptic Survey Telescope. We thank the LSST Project for making their code available as free software at http://dm.lsst.org.

The Pan-STARRS1 Surveys (PS1) have been made possible through contributions of the Institute for Astronomy, the University of Hawaii, the Pan-STARRS Project Office, the Max-Planck Society and its participating institutes, the Max Planck Institute for Astronomy, Heidelberg and the Max Planck Institute for Extraterrestrial Physics, Garching, The Johns Hopkins University, Durham University, the University of Edinburgh, Queens University Belfast, the Harvard-Smithsonian Center for Astrophysics, the Las Cumbres Observatory Global Telescope Network Incorporated, the National Central University of Taiwan, the Space Telescope Science Institute, the National Aeronautics and Space Administration under Grant No. NNX08AR22G issued through the Planetary Science Division of the NASA Science Mission Directorate, the National Science Foundation under Grant No. AST-1238877, the University of Maryland, and Eotvos Lorand University (ELTE) and the Los Alamos National Laboratory.

Some of the data presented in this paper were obtained from the Mikulski Archive for Space Telescopes (MAST). STScI is operated by the Association of Universities for Research in Astronomy, Inc., under NASA contract NAS5-26555. Support for MAST for non-HST data is provided by the NASA Office of Space Science via grant NNX13AC07G and by other grants and contracts.

Based on observations made with the NASA Galaxy Evolution Explorer. GALEX is operated for NASA by the California Institute of Technology under NASA contract NAS5-98034.

This research has made use of the NASA/IPAC Infrared Science Archive, which is operated by the Jet Propulsion Laboratory, California Institute of Technology, under contract with the National Aeronautics and Space Administration.

This research has made use of the VizieR catalog access tool, CDS, Strasbourg, France.

Software: Astropy (Astropy Collaboration et al. 2013; Price-Whelan et al. 2018), matplotlib (Hunter 2007), SciPy (Virtanen et al. 2020), the IPython package (Perez & Granger 2007), NumPy (Van Der Walt et al. 2011), pandas (McKinney 2010, 2011), Astroquery (Ginsburg et al. 2019), extinction (Barbary 2021).

ORCID iDs

Erin Kado-Fong https://orcid.org/0000-0002-0332-177X
Chang-Goo Kim https://orcid.org/0000-0003-2896-3725
Jenny E. Greene https://orcid.org/0000-0002-5612-3427
Lachlan Lancaster https://orcid.org/0000-0002-0041-4356

References

Aihara, H., Allende Prieto, C., An, D., et al. 2011, ApJS, 193, 29
Aihara, H., AlSayyad, Y., Ando, M., et al. 2019, PASJ, 71, 114
Aihara, H., AlSayyad, Y., Ando, M., et al. 2022, PASJ, 74, 247
Amorin, R., Munoz-Tunon, C., Aguerri, J. A. L., & Planesas, P. 2016, A&A, 588, A23
Amorisco, N. C., & Loeb, A. 2016, MNRAS, 459, L51
Astropy Collaboration, Robitaille, T. P., Tollerud, E. J., et al. 2013, A&A, 558, A33
Bakes, E. L. O., & Tielens, A. G. G. M. 1994, ApJ, 427, 822
Barbary, K. 2021, Extinction: Dust extinction laws, Astrophysics Source Code Library, record ascl:2102.026
Barrera-Ballesteros, J. K., Sanchez, S. F., Heckman, T., et al. 2021, MNRAS, 503, 3643
Beasley, M. A., & Trujillo, I. 2016, ApJ, 830, 23
Behroozi, P., Wechsler, R. H., Hearin, A. P., & Conroy, C. 2019, MNRAS, 488, 3143
Bellstedt, S., Robotham, A. S. G., Driver, S. P., et al. 2021, MNRAS, 503, 3309
Berg, D. A., Skillman, E. D., Marble, A. R., et al. 2012, ApJ, 754, 98
Bigiel, F., Leroy, A., Walter, F., et al. 2008, AJ, 136, 2846
Bigiel, F., Leroy, A. K., Walter, F., et al. 2011, ApJL, 730, L13
Blanton, M. R., Kazin, E., Muna, D., Weaver, B. A., & Price-Whelan, A. 2011, AJ, 142, 31
Bolatto, A. D., Wolfire, M., & Leroy, A. K. 2013, ARA&A, 51, 207
Bradford, J. D., Geha, M. C., & Blanton, M. R. 2015, ApJ, 809, 146
Brinchmann, J., Charlot, S., Heckman, T. M., et al. 2004, arXiv:astro-ph/0406220
Calzetti, D. 2013, in Secular Evolution of Galaxies, ed. J. Falcón-Barroso & J. H. Knapen (Cambridge: Cambridge Univ. Press), 419
Carlsten, S. G., Greene, J. E., Beaton, R. L., Danieli, S., & Greco, J. P. 2022, ApJ, 933, 47
Carlsten, S. G., Greene, J. E., Greco, J. P., Beaton, R. L., & Kado-Fong, E. 2021, ApJ, 922, 267
Chan, T. K., Keres, D., Wetzel, A., et al. 2018, MNRAS, 478, 906
Child, H. L., Habib, S., Heitmann, K., et al. 2018, ApJ, 859, 55
Cigan, P., Young, L. M., Gomez, H. L., et al. 2021, AJ, 162, 83
Conroy, C., & Gunn, J. E. 2010, ApJ, 712, 833
Conroy, C., Gunn, J. E., & White, M. 2009, ApJ, 699, 486
Dalcanton, J. J., Spergel, D. N., Gunn, J. E., Schmidt, M., & Schneider, D. P. 1997, AJ, 114, 635
Danieli, S., van Dokkum, P., Conroy, C., Abraham, R., & Romanowsky, A. J. 2019, ApJL, 874, L12
Danieli, S., van Dokkum, P., Trujillo-Gomez, S., et al. 2022, ApJL, 927, L28
Dashyan, G., & Dubois, Y. 2020, A&A, 638, A123
de los Reyes, M. A. C., & Kennicutt, R. C. J. 2019, ApJ, 872, 16
Dekel, A., & Silk, J. 1986, ApJ, 303, 39
Di Cintio, A., Brook, C. B., Dutton, A. A., et al. 2017, MNRAS, 466, L1
El-Badry, K., Wetzel, A., Geha, M., et al. 2016, ApJ, 820, 131
Fielding, D., Quataert, E., & Martizzi, D. 2018, MNRAS, 481, 3325
Foreman-Mackey, D., Hogg, D. W., Lang, D., & Goodman, J. 2013, PASP, 125, 306
Gao, Y., Gu, Q., Shi, Y., et al. 2022, A&A, 661, A136
Gault, L., Leisman, L., Adams, E. A. K., et al. 2021, ApJ, 909, 19
Geha, M., Blanton, M. R., Yan, R., & Tinker, J. L. 2012, ApJ, 757, 85
Ginsburg, A., Sipocz, B. M., Brasseur, C. E., et al. 2019, AJ, 157, 98
Girichidis, P., Naab, T., Hanasz, M., & Walch, S. 2018, MNRAS, 479, 3042
Gong, M., Ostriker, E. C., Kim, C. -G., & Kim, J. -G. 2020, ApJ, 903, 142
Greco, J. P., Goulding, A. D., Greene, J. E., et al. 2018a, ApJ, 866, 112
Greco, J. P., Greene, J. E., Strauss, M. A., et al. 2018b, ApJ, 857, 104
Greene, J. E., Greco, J. P., Goulding, A. D., et al. 2022, arXiv:2204.11883
Herrera-Camus, R., Bolatto, A., Wolfire, M., et al. 2017, ApJ, 835, 201
Holmberg, E. 1958, MeLuS, 136, 1
Hopkins, P. F., Wetzel, A., Keres, D., et al. 2018, MNRAS, 480, 800
Hu, C. -Y. 2019, MNRAS, 483, 3363
Hunter, D. A., Ficut-Vicas, D., Ashley, T., et al. 2012, AJ, 144, 134
Hunter, J. D. 2007, CSE, 9, 90
Iffrig, O., & Hennebelle, P. 2015, A&A, 576, A95
Janowiecki, S., Jones, M. G., Leisman, L., & Webb, A. 2019, MNRAS, 490, 566
Jiang, F., Dekel, A., Freundlich, J., et al. 2019, MNRAS, 487, 5272
Jimmy, Tran, K. V., Saintonge, A., et al. 2015, ApJ, 812, 98
Kado-Fong, E., Greene, J. E., Huang, S., et al. 2020, ApJ, 900, 163
Kado-Fong, E., Greene, J. E., Huang, S., & Goulding, A. 2022, arXiv:2209.05492
Kado-Fong, E., Petrescu, M., Mohammad, M., et al. 2021, ApJ, 920, 72
Kannan, R., Vogelsberger, M., Marinacci, F., et al. 2019, MNRAS, 485, 117
Kauffmann, G., Heckman, T. M., Simon White, D. M., et al. 2003, MNRAS, 341, 33
Kennicutt, R. C., Calzetti, D., Aniano, G., et al. 2011, PASP, 123, 1347
Kepley, A. A., Leroy, A. K., Johnson, K. E., Sandstrom, K., & Chen, C. H. R. 2016, ApJ, 828, 50
Kim, C.-G., Kim, W. -T., & Ostriker, E. C. 2011, ApJ, 743, 25
Kim, C.-G., & Ostriker, E. C. 2015, ApJ, 815, 67
Kim, C.-G., & Ostriker, E. C. 2017, ApJ, 846, 133
Kim, C.-G., Ostriker, E. C., & Kim, W. -T. 2013, ApJ, 776, 1
Kim, C.-G., Ostriker, E. C., & Raileanu, R. 2017, ApJ, 834, 25
Kim, J.-G., Ostriker, E. C., & Filippova, N. 2021, ApJ, 911, 128
Kong, D., Kaplinghat, M., Yu, H. -B., Fraternali, F., & Mancera Piña, P. E. 2022, ApJ, 936, 166
Kroupa, P. 2001, MNRAS, 322, 231
Krumholz, M. R., McKee, C. F., & Tumlinson, J. 2009, ApJ, 699, 850
Lancaster, L., Ostriker, E. C., Kim, J. -G., & Kim, C. -G. 2021, ApJL, 922, L3
Lee, H., Skillman, E. D., Cannon, J. M., et al. 2006, ApJ, 647, 970
Leisman, L., Haynes, M. P., Janowiecki, S., et al. 2017, ApJ, 842, 133
Leroy, A. K., Schinnerer, E., Hughes, A., et al. 2021, ApJS, 257, 43
Leroy, A. K., Walter, F., Brinks, E., et al. 2008, AJ, 136, 2782
Liao, S., Gao, L., Frenk, C. S., et al. 2019, MNRAS, 490, 5182
Mancera Piña, P. E., Fraternali, F., Adams, E. A. K., et al. 2019, ApJL, 883, L33
Mancera Piña, P. E., Fraternali, F., Oman, K. A., et al. 2020, MNRAS, 495, 3636
Mancera Piña, P. E., Fraternali, F., Oosterloo, T., et al. 2022, MNRAS, 512, 3230
Martizzi, D., Faucher-Giguere, C. -A., & Quataert, E. 2015, MNRAS, 450, 504
McGaugh, S. S., Bothun, G. D., & Schombert, J. M. 1995, AJ, 110, 573
McKinney, W. 2010, in Proc. of the 9th Python in Sci. Conf., 445, Austin, TX (Austin, TX: SciPy), 51
McKinney, W. 2011, Python for High Performance and Scientific Computing, 14, 1
Navarro, J. F., Frenk, C. S., & White, S. D. M. 1997, ApJ, 490, 493
Oh, S. -H., de Blok, W. J. G., Brinks, E., Walter, F., & Kennicutt, R. C. J. 2011, AJ, 141, 193
Oku, Y., Tomida, K., Nagamine, K., Shimizu, I., & Cen, R. 2022, ApJS, 262, 9
Orr, M. E., Hayward, C. C., & Hopkins, P. F. 2019, MNRAS, 486, 4724
Ostriker, E. C., & Kim, C. -G. 2022, ApJ, 936, 137
Ostriker, E. C., McKee, C. F., & Leroy, A. K. 2010, ApJ, 721, 975
Ostriker, E. C., & Shetty, R. 2011, ApJ, 731, 41
Ostriker, E. C., Stone, J. M., & Gammie, C. F. 2001, ApJ, 546, 980
Peng, E. W., & Lim, S. 2016, ApJL, 822, L31
Perez, F., & Granger, B. E. 2007, CSE, 9, 21
Price-Whelan, A. M., Sipocz, B. M., Gunther, H. M., et al. 2018, AJ, 156, 123
Saifollahi, T., Trujillo, I., Beasley, M. A., Peletier, R. F., & Knapen, J. H. 2021, MNRAS, 502, 5921
Sales, L. V., Navarro, J. F., Penafiel, L., et al. 2020, MNRAS, 494, 1848
Salim, S., Rich, R. M., Charlot, S., et al. 2007, ApJS, 173, 267
Sánchez Almeida, J., Olmo-García, A., Elmegreen, B. G., et al. 2018, ApJ, 869, 40
Sandage, A., & Binggeli, B. 1984, AJ, 89, 919
Schruba, A., Leroy, A. K., Walter, F., et al. 2011, AJ, 142, 37
Schruba, A., Leroy, A. K., Walter, F., et al. 2012, AJ, 143, 138
Shivaei, I., Popping, G., Rieke, G., et al. 2022, ApJ, 928, 68
Silk, J. 1997, ApJ, 481, 703
Smith, M. C., Bryan, G. L., Somerville, R. S., et al. 2021, MNRAS, 506, 3882
Sun, J., Leroy, A. K., Ostriker, E. C., et al. 2020, ApJ, 892, 148
Utomo, D., Bolatto, A. D., Wong, T., et al. 2017, ApJ, 849, 26
Van Der Walt, S., Colbert, S. C., & Varoquaux, G. 2011, CSE, 13, 22
van Dokkum, P., Danieli, S., Cohen, Y., et al. 2018, Natur, 555, 629
van Dokkum, P., Wasserman, A., Danieli, S., et al. 2019, ApJ, 880, 91
van Dokkum, P. G., Abraham, R., Merritt, A., et al. 2015, ApJL, 798, L45
Van Nest, J. D., Munshi, F., Wright, A. C., et al. 2022, ApJ, 926, 92
Virtanen, P., Gommers, R., Oliphant, T. E., et al. 2020, NatMe, 17, 261
Weingartner, J. C., & Draine, B. T. 2001, ApJS, 134, 263
Wolfire, M. G., McKee, C. F., Hollenbach, D., & Tielens, A. G. G. M. 2003, ApJ, 587, 278
Wright, A. C., Tremmel, M., Brooks, A. M., et al. 2021, MNRAS, 502, 5370
Yagi, M., Koda, J., Komiyama, Y., & Yamanoi, H. 2016, ApJS, 225, 11